Pergamon

Geochimica et Cosmochimica Acta, Vol. 67, No. 23, pp. 4597–4619, 2003

0016-7037/03 $30.00 + .00

doi:10.1016/S0016-7037(03)00414-9

Dating ultra-deep mine waters with noble gases and ^{36}Cl, Witwatersrand Basin, South Africa

J. LIPPMANN,*[,1,†] M. STUTE,[1,2] T. TORGERSEN,[3] D. P. MOSER,[4] J. A. HALL,[5] L. LIN,[5] M. BORCSIK,[5] R. E. S. BELLAMY,[6] and T. C. ONSTOTT[5]

[1]Lamont-Doherty Earth Observatory of Columbia University, Palisades NY 10964, USA
[2]Barnard College, New York, NY 10027, USA
[3]Department of Marine Sciences, University of Connecticut, Groton, CT 06340, USA
[4]Pacific Northwest National Laboratories, Richland, WA 99352, USA
[5]Department of Geosciences, Princeton University, Princeton, NJ 08544, USA
[6]Geology Dept Beatrix Mine, P O Box 2823, Welkom, 9460 South Africa

(*Received May* 15, 2002; *accepted in revised form May* 22, 2003)

Abstract—Concentrations and isotopic ratios of dissolved noble gases, ^{36}Cl, δD and δ^{18}O in water samples from the ultra-deep gold mines (0.718 to 3.3 km below the surface) in the Witwatersrand Basin, South Africa, were investigated to quantify the dynamics of these ultra deep crustal fluids. The mining activity has a significant impact on the concentrations of dissolved gases, as the associated pressure release causes the degassing of the fissure water. The observed under saturation of the atmospheric noble gases in the fissure water samples (70–98%, normalized to ASW at 20°C and 1013 mbar) is reproduced by a model that considers diffusive degassing and solubility equilibration with a gas phase at sampling temperature. Corrections for degassing result in ^{4}He concentrations as high as $1.55 \cdot 10^{-1}$ cm^{3}STP^{4}He g^{-1}, ^{40}Ar/^{36}Ar ranging between 806 and 10 331, and ^{134}Xe/^{132}Xe and ^{136}Xe/^{132}Xe ratios above 0.46 and 0.44, respectively. Corrected $^{134(136)}$Xe/^{132}Xe and $^{134(136)}$Xe/^{4}He-ratios are consistent with their production ratios, whereas the nucleogenic ^{4}He/^{40}Ar, and $^{134(136)}$Xe/^{40}Ar ratios generally indicate that these gases are produced in an environment with an average [U + Th]/K-content 2–3 times above that of crustal average. In two scenarios, one considering only accumulation of in situ produced noble gases, the other additionally crustal flux components, the model ages for 14 individual water samples range from 13 to 168 Ma and from 1 to 23 Ma, respectively.

The low ^{36}Cl-ratios of $(4–37) \cdot 10^{-15}$ and comparatively high ^{36}Cl-concentrations of $(8–350) \cdot 10^{-15}$ atoms ^{36}Cl l^{-1} reflect subsurface production in secular equilibrium indicating an age in excess of 1.5 Ma or 5 times the half-life of ^{36}Cl.

In combination, the results suggest residence times of the fluids in fissures in this region (up to 3.3 km depth) are of the order of 1–100 Ma. We cannot exclude the possibility of mixing and that small quantities of younger water have been mixed with the very old bulk. *Copyright © 2003 Elsevier Ltd*

1. INTRODUCTION

The diversity and history of life on Earth is still one of the most fascinating questions. Researchers are pushing frontiers by looking at life forms in extreme environments, such as hydrothermal vents (Karl, 1995), arctic ice (Karl et al., 1999; Priscu et al., 2001), deep continental crust (Pedersen, 1997), other planets (Boston et al., 1992), or at organisms trapped and isolated over geological time scales in amber or rock salt (Cano and Borucki, 1995; Vreeland et al., 2000). One of the newest research areas is the ultra deep gold mines in South Africa, the deepest continental sites on Earth that provide access to scientists.

Pressurized, saline fissure waters were sampled from flowing roof boreholes, cover boreholes and fractures associated with subvertical dykes and faults in deep mines ranging in depth from 0.7 to 3.3 km. The fluids collected have been shown to host living microbes with diverse phylogenetic and phenotypic properties (Kieft et al., 1999; Moser et al., 2001; Moser et al., 2002; Takai et al., 2002). To better characterize the evolution of these microbes, an understanding of the dynamics of the fluids is necessary. Previous δD and δ^{18}O and hydrochemical analyses of the fissure water samples indicate that they are meteoric and, hence, originally derived from the surface but have undergone significant enrichment in dissolved inorganic species (Duane et al., 1997; Takai et al., 2001; 2002). Residence times of these waters are expected to be very large.

The purpose of this study is to characterize the fluid residence times in this hydrogeological environment, using dissolved noble gas concentrations, their isotope ratios, as well as ^{36}Cl, δD and δ^{18}O data.

2. GEOLOGY OF THE WITWATERSRAND BASIN

The Witwatersrand Basin is well known for its exceptional gold mineralization and has thus been intensively investigated. Since the first mention of mining of gold in 1836 (Whiteside et al., 1986), about 45 000 tons of gold (Handley, 1990) and 150 000 tons of uranium have been produced from the Witwatersrand and Ventersdorp supergroups (Robb and Meyer, 1995).

The basin lies within the Archaean Kaapvaal Craton of South Africa (Fig. 1a and b) and formed episodically between about 3074 Ma and 2714 Ma (Robb and Meyer, 1995) as a result of

* Author to whom correspondence should be addressed (Lippmann@gfz-potsdam.de).
† *Present address:* GeoForschungsZentrum (GFZ) Potsdam, Germany

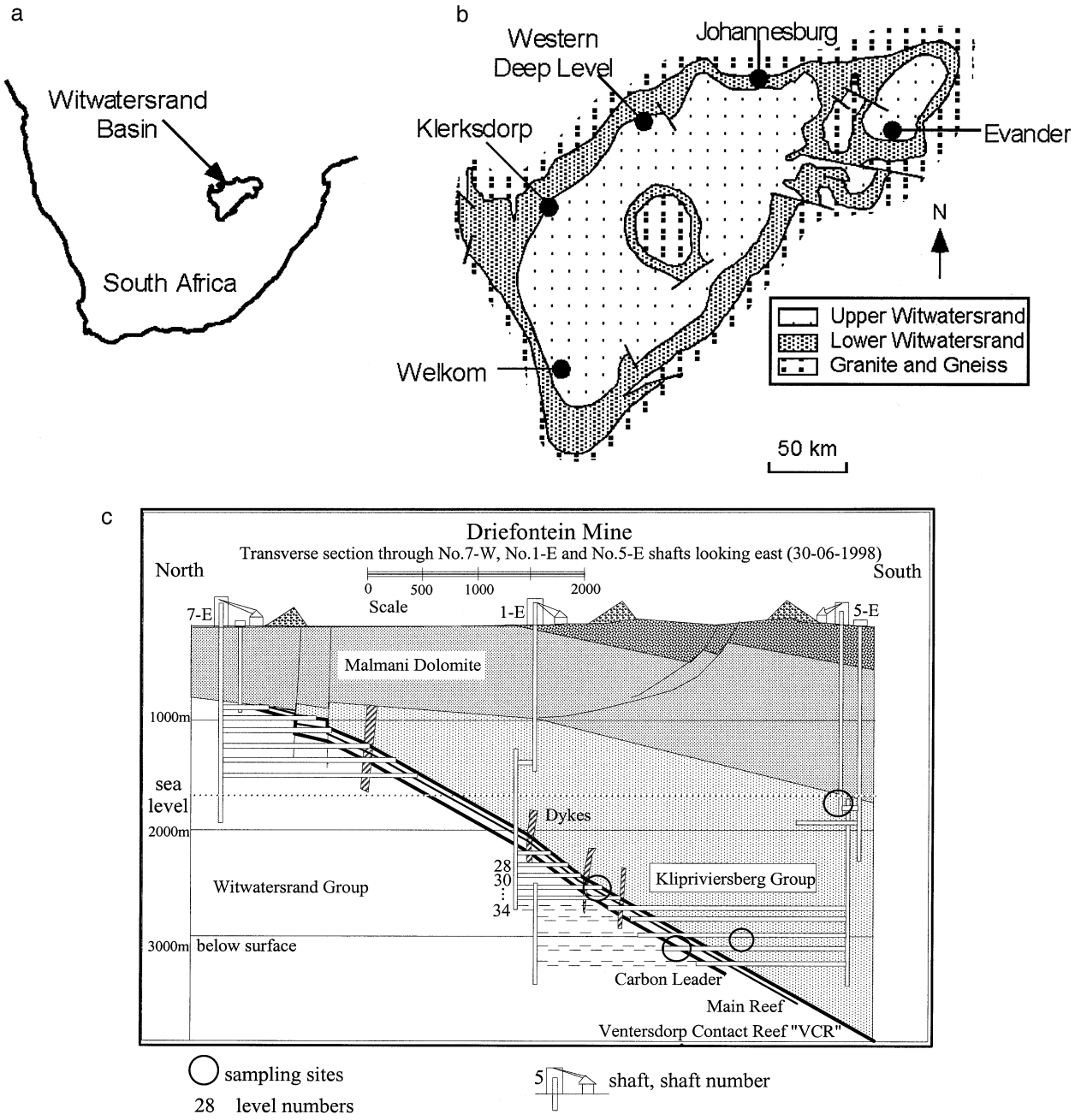

Fig. 1. **a and b:** The Witwatersrand Basin in southern Africa (a), and the schematic geology of the Witwatersrand basin (b): The four gold mines from which the samples were obtained are Beatrix near Welkom in the south, Kloof and Driefontein near Western Deep Levels in the north and Evander Gold Mine in the east of the basin (source: Reimold et al., 1995). **c:** Geological cross section of the Witwatersrand basin at its northern margin at Driefontein mine. This cross-section gives a general overview of the geology of the sampling sites for mine samples. The Ventersdorp Contact Reef (VCR) is the contact between the Witwatersrand Supergroup and the Ventersdorp Supergroup (here the Klipriviersberg lava). The Carbon Leader occurs approximately 200 m below this contact. The Malmani Dolomite Supergroup (part of the Transvaal Supergroup) is present in the Kloof and Driefontein mines and has a thickness of 900 to 2000 m. At Evander Goldfields, the Transvaal Supergroup is present only in the northern part of the mine. In the south, the dolomite has been removed in pre-Karoo erosion. At Beatrix mines, the dolomite (Transvaal Supergroup) does not exist and the Ventersdorp lavas are covered directly by and 400 m of Karoo sediments (source: Driefontein Consolidated Limited, 1998)

several discrete tectonomagmatic events (deWitt et al., 1992). The basin is 320 km along a northeasterly axis by 160 km along a northwesterly strike. The Witwatersrand Supergroup is comprised of approximately 7000 m of terrigenous sediment. The elevation ranges between 1340 m and 1820 m. The Vredefort Dome, near the center of the basin, formed as the results of a

Table 1. U, Th and K concentrations of rock samples.

Formation	Lithology	No. of samples	ρ_{rock}	U [ppm]	Th [ppm]	K	$(^4He/^{40}Ar)_{rad}$
				[ppm]	[ppm]	[%]	
Carbon Leader Reef, Driefontein	conglomerate		*2.6**	1.8%	–	0.3*	183.689
Ventersorp Contact Reef	conglomerate	1	*2.6**	676,0	16,5	0,05	41.636
Beatrix Reef, average	conglomerate	4	*2.6**	1127,0	81,2	0,55	6.383
Kimberley Reef, Evander	conglomerate	2	*2.6**	247,0	17,5	0,34	2.262
Beatrix, average	quartzite	10	*2.6**	74 ± 75	7.3 ± 7.5	1,34	173
Beatrix, selected hanging & foot	quartzite	7	*2.6**	4,7	31,2	1,32	29
Beatrix, quartzite, lowest in U	quartzite	1	*2.6**	3,0	2,7	1,69	7
Kliprieviersberg Lava, Kloof	lava	1	*2,85*	419,0	<0.05	1,53	838
Eldorado Group, Evander	quartzite	2	*2.6**	211,0	3,9	0,46	1.411
Mooidraai Dolomite	dolomite	1	*2,85*	17,6	2,0	0,16	346
Average Upper Crust (Taylor and McLennan, 1985)				2,8	10,6	3,4	4,9
Sandstone (Ballentine et al., 1994)				4,5	7,4	1,8	10,8

* Estimated values. Gravimetrically determined porosities range from 0.1 to 0.8%, values reported for the Mooidraai Dolomite range from 14% (weathered) to below 2% (Vegter, 1992). 1.8% U for the Carbon Leader is lowest reported value: Hallbauer (1986) analyzed and reported (1.8–7.0)%; Calculated $(^4He/^{40}Ar)_{rad}$-ratio are based on the stated U, Th and K contents.

meteorite impact 2025 Ma ago (Whiteside et al., 1986; Grieve et al., 1990; Leroux et al., 1994). The Witwatersrand Supergroup is underlain by either the 3450 Ma granite-greenstone terrain or by the 3074 Ma volcano-sedimentary Dominion Group; it is overlain by the volcanics of the Ventersdorp Supergroup (2714 Ma). The combined sequence of the Dominion, the Witwatersrand and the Ventersdorp strata is also called the Witwatersrand Triad. The Triad is partially covered by the sediments and volcanics of the Transvaal Supergroup (2560 Ma). The southern and eastern portions of the Witwatersrand Basin are overlain by the Karoo System (254 to 190 Ma).

In this study, water samples from four different mines in the Witwatersrand Basin were analysed: Evander Goldfield is located approximately 120 km east-south-east of Johannesburg at the eastern extension of the Witwatersrand Basin (Fig. 1a,b); Beatrix gold mine is located approximately 340 km south-west of Johannesburg at the southern end of the Witwatersrand Basin; Kloof and Driefontein gold mines are located in the northern margin of the basin, near Carletonville.

A geological cross section of the northern margin of the Witwatersrand Basin near Driefontein gold mine (Fig. 1c) depicts the stratigraphic succession encountered at all four gold mines, although structural details vary between the mines. Except for the Ventersdorp Contact Reef (VCR), all exploited gold and uranium reefs in the area are within the Central Rand Group. This is a subgroup of the Witwatersrand Supergroup consisting mostly of quartzite and conglomerates and was deposited some time after 2914 Ma and before 2714 Ma years (Armstrong et al, 1991; Robb et al., 1997). The Ventersdorp Contact Reef (VCR) is located at the unconformity between the Witwatersrand and the overlying Ventersdorp Supergroup. The rock formations of the Witwatersrand Supergroup are mostly quartzites and conglomerates; the overlying Ventersdorp Supergroup are mostly lavas. The Transvaal sequence consists primarily of a thick dolomitic unit, which acts as an aquifer in large areas of the basin, especially where the dolomite was exposed to weathering processes before being buried under the terrigenous sediments of the Transvaal Supergroup. The Karoo System in this region forms isolated pockets of shale.

Evander Goldfield

In most of the Evander Goldfield, the Transvaal and upper parts of the Witwatersrand Supergroup (Central Rand Group) have been partially removed by pre-Karoo erosion. Dolomite exists only in the northern part of the Evander Goldfield. The degree of faulting and structural dislocation within the Evander Goldfield is greater than that encountered at the other three gold mines (Tweedie E. B., 1986). The hydrology of the Evander Goldfield has been studied and reported by Brand (1986).

Beatrix Gold Mine

At the Beatrix gold mine the Witwatersrand Supergroup lies beneath 400 to 800 m of carboniferous Karoo sediments (Tweedie K. A. M., 1986). The Beatrix Reef is a quartz-pebble conglomerate up to 130 cm thick with moderate gold and generally low uranium concentrations.

Kloof and Driefontein Gold Mines

Kloof and (East and West) Driefontein gold mines are located in the West Rand portion of the basin, where northerly trending, 1.4 Ga Pilansberg dykes have compartmentalized the Transvaal dolomitic aquifer and the underlying Witwatersrand and Ventersdorp sequences. These dykes act as conduits for vertical fluid recharge from the overlying dolomitic aquifer. At Kloof, the VCR and the Main Reef are mined, whereas, at Driefontein the VCR and Carbon Leader are mined. The latter is significantly enriched in U (see Table 1).

3. MATERIAL AND METHODS

3.1. Basic Principles

The atmosphere is the major source of noble gases dissolved in ground water. In addition, the isotopes ^3He, ^4He, ^{40}Ar, ^{21}Ne, ^{22}Ne, ^{134}Xe, and ^{136}Xe are produced in the host rock by decay of U, Th, and K and secondary nucleogenic production processes. (Hereafter, we will refer to all these isotopes as ‘nucleogenic’ noble gas isotopes regardless of their specific mode of production.) They are released from the minerals and rocks into the corresponding pore water by recoil during their production, by diffusion or by reaction of the minerals and rocks

(Torgersen, 1980; Andrews, 1985; Solomon et al., 1996). In addition to this in-situ production and accumulation of noble gases, A_{is}, crustal fluxes, J_i, contribute to the total dissolved concentrations (e.g., Torgersen and Ivey, 1985; Stute et al., 1992b).

For more than three decades, the study of the noble gas concentrations in water samples has improved our understanding of large hydrogeological systems. Mazor (1972) studied dissolved noble gases in thermal ground waters of the Jordan Rift Valley in Israel and found the concentration of dissolved noble gases did not reflect the sampling temperature. He suggested that ground water can be used as an archive of palaeoclimate, as it appeared to retain this information over many thousands of years. The first palaeotemperature record was established for the Bunter Sandstone of England (Andrews and Lee, 1979), and followed by numerous noble gas in palaeoclimate studies (e.g., Heaton, 1981; Rudolph et al., 1983; Stute et al., 1992a; Stute et al., 1995a, 1995b, and Aeschbach-Hertig et al. 1999). Noble gas studies have also contributed significantly to the understanding of the role of deep circulating groundwater in hydrocarbon accumulation (Bosch and Mazor, 1988; Ballentine et al., 1991; Pinti and Marty, 1995; and Ballentine et al., 1996) and for migration and storage (Elliot et al., 1993; Ballentine et al., 1994 and Torgersen and Kennedy, 1999). Groundwater accumulations of nucleogenic noble gases and their concentration distributions have been used to estimate residence times (e.g., Torgersen, 1980; Andrews, 1985; Stute et al., 1992a; Solomon et al., 1996; Pinti and Marty, 1997; Castro et al., 2000). More recently, determination of dissolved noble gas concentrations in the pore water of freshly drilled rock cores has provided information on hydrodynamic properties of low permeability formations, such as diffusion coefficients in pore spaces, and the permeability and connectivity of the pore space (Osenbrück et al., 1998; Lippmann, 1998; Rübel et al., 2002).

Although the production and release of ^{4}He and ^{40}Ar from minerals to the fluid phase at the microscopic scale is well understood (Torgersen, 1980; Lippold and Weigel, 1988; Martel et al., 1990), the factors that control this release on a regional scale are not as well constrained (Tolstikhin et al., 1996). The release rate is greater at higher temperatures and may equal the production rate at temperatures of 130 to 230°C (Klemd et al., 1989). Furthermore, the ratio of nucleogenic noble gas isotopes in pore fluids, e.g., ^{4}He/^{40}Ar, can be considerably influenced by rock-fracturing and subsequent release of accumulated noble gases (Torgersen and O'Donnell, 1991). The measured ratios of these nucleogenic noble gases in the fluid phase may differ significantly from their production ratio as fractionation occurs during the degassing of the fractured blocks.

The utility of Chloride as a hydrological tracer has been greatly extended by the recognition that the element has a long-lived radioactive isotope: ^{36}Cl (see Fabryka-Martin et al., 1987; Fontes, 1989, and Torgersen et al., 1991). This isotope is produced in the higher atmosphere by interaction with cosmic rays. The atmospheric deposition rate depends on the geomagnetic latitude of the investigation area, the annual precipitation rate and the Cl-concentration in the precipitation. For South Africa, deposition is about 12–18 [atoms m^{-2} s^{-1} (Lal and Peters, 1967). The ^{36}Cl half-live is 301 ka. ^{36}Cl is analysed by AMS (Accelerator Mass Spectrometry). After about 5 half-lifes (15 Ma) the signal typically is no longer distinguishable from background ratios.

3.2. Sample Collection

In 1998 and 2001, water-bearing fissures intersected by mining operations were sampled for noble gases at 16 exploration boreholes accessed in the deep mines. Four fissure water samples were collected from Evander gold mine covering a depth range of 1500 m to 1800 m. Eight fissure water samples, one core sample and one tap water sample were collected from Beatrix gold mine. The fissure and pore water samples cover a depth range of 718 m to 1400 m. Four fissure waters each were collected from Kloof and Driefontein, one ground water and one waste water sample were collected at Driefontein, covering a depth range of 980 m to 3300 m. For more details on the individual samples, see Table A1 in the Appendix.

The 1 to 4 inch boreholes used to gain access to the fissure waters were sealed with an adjustable packing system specially designed to enable sterile water sampling (Moser et al., 2002). The 20-mL copper tube sampling containers were connected with pressure-tight PVC tubing to the packer, and on the other end to a valve for controlling and reducing flow rate. After flushing the tube with sample water, the valve was incrementally closed and the copper tube was sealed by crimping it with stainless steel clamps at both ends. Considerable efforts were made to avoid degassing during sampling. Nevertheless, in some cases the water pressure in the formation was higher than the maximum pressure tolerance of the packer/sampling system. Thus, not all dissolved gases could be kept in solution during sampling. Additionally, because of fracturing around stopes and pressure release during and after mining activity, one might expect degassing to occur even far back in the formation. In some cases, where the boreholes dipped downwards into the hanging or footwall formations, the outflow of the fissure water resembled geyser-like eruptions of gas and hot water mixtures.

The ground water sample was taken from a valved borehole that connects with a service water reservoir (Internal Pump Compartment) and is fed by the regional aquifer. The single pore water sample (BE19BWBhDD13677) was taken 2–3 h after core drilling of an exploration borehole at the Beatrix mine. A fresh, 8 cm core segment was immediately transferred into a stainless steel container, repeatedly evacuated and flushed with pure nitrogen (grade 5.0) and finally sealed vacuum tight, according to the method described by Osenbrück et al. (1998).

For ^{36}Cl-isotope measurements, 1 L of water was collected in a glass bottle with plastic poly seal caps.

3.3. Analytical Methods

3.3.1. Noble gases

The noble gas concentrations were determined on a MAP215-50 noble gas mass spectrometer using the methods outlined by Stute et al., (1995a). The precision of the absolute concentration measurement is ±2% for ^{40}Ar, ^{84}Kr and ^{132}Xe. As the ^{4}He concentrations were 2–6 orders of magnitude above ASW, the concentration was determined with a spinning rotor gas friction manometer with an estimated uncertainty of about ±10%. The precision of the ^{3}He/^{4}He isotope ratio measurement was about (1–3) %; the reproducibility of isotope ratios of air standards was better than 1% for ^{40}Ar/^{36}Ar and 2–4% for Xe isotopes. For Ne, 2% precision is typical for regular water samples (very near saturation samples where the signal of the ^{20}Ne-peak is covered by the range of the standards and where the correction applied for the $^{40}Ar^{++}$-contribution on mass 20 is checked by water standard measurements). Because the fissure water samples were significantly undersaturated with respect to atmospheric noble gases, the precision of the ^{20}Ne measurement is not as good as for regular water samples (the mass 20 signal was about 1 order of magnitude below the range covered by air standard measurements). Additionally, as the fissure water samples contained significant radiogenic ^{40}Ar, the $^{40}Ar^{++}$correction on mass 20 is not cross-checked by standard measurements. Therefore, the ^{21}Ne/^{20}Ne and ^{22}Ne/^{20}Ne-ratios have a large uncertainty, sometimes as high as 200%. We discard all Ne-ratios from this paper due to the low quality of the data.

The noble gases dissolved in the pore water of the freshly drilled cores are quantitatively released by molecular diffusion out of the pore water into the container volume of about 450 cm^3 within about a month (Osenbrück et al., 1998). Subsequently, the gases are transferred into the preparation line of the MAP215-50 for measurement. The water content of the core sample is determined gravimetrically by drying at 100°C for a minimum of 24 h.

3.3.2. ^{36}Cl/Cl

Cl was precipitated as AgCl in a clean lab at LDEO according to guidelines issued by the Prime Lab, Purdue University (personal communication). As most samples have low Cl-concentrations (<2 g/L), they were first preconcentrated on anion exchange resin (1-X8, 100–200 mesh, Eichrom Technologies, IL, #A8B500-NCL) and sulfate was precipitated with $Ba(NO_3)_2$. After concentration on a second resin column, Cl was precipitated as AgCl (30–40 mg) and oven dried at 60°C. The ^{36}Cl/^{35}Cl ratio of the AgCl target was analysed by accelerator mass spectrometry at the PRIME laboratory, Purdue University using the method of Elmore et al. (1979). As a control for ^{36}Cl-contamination during the preconcentration and AgCl precipitation pro-

Table 2. Measured noble gas concentrations and isotope ratios.

Sample	^{4}He [10^{-4}]	^{20}Ne [10^{-7}]	^{40}Ar [10^{-4}]	^{84}Kr [10^{-8}]	^{132}Xe [10^{-9}]	^{3}He/^{4}He [10^{-8}]	R/R$_a$	^{40}Ar/^{36}Ar	^{134}Xe/^{132}Xe	^{136}Xe/^{132}Xe	^{20}Ne/^{36}Ar	C_{Ne}/C_{Ne}^0
						cm^3 g^{-1} (STP)						
BE19BWBhDD13677	184.80	2.77	10.46	4.08	2.38	3.34	0.024	900 ± 36	0.3919 ± 0.002	0.3378 ± 0.003	0.24 ± 0.01	1.65
BE16FW-GDW #1	5.90	0.08	1.81	0.76	0.58	3.55	0.026	1392 ± 56	0.3964 ± 0.007	0.3412 ± 0.009	0.06 ± 0.01	0.05
BE16FW-GDW #3	4.28	0.08	1.90	1.11	0.76	3.23	0.023	759 ± 30	0.3922 ± 0.003	0.3360 ± 0.004	0.03 ± 0.00	0.05
BE23FW-A4RD	12.92	0.29	3.42	1.29	0.83	3.28	0.024	1291 ± 52	0.3936 ± 0.005	0.3371 ± 0.007	0.11 ± 0.01	0.17
BE24FW-C17W18 #2	3.64	0.10	1.69	0.68	0.47	3.05	0.022	1372 ± 55	0.3959 ± 0.004	0.3389 ± 0.007	0.08 ± 0.01	0.06
BE325FW-CTS	12.62	0.11	3.63	0.86	0.58	2.58	0.019	2309 ± 92	0.3964 ± 0.007	0.3411 ± 0.002	0.07 ± 0.01	0.06
BE327FW-CTS	19.76	0.20	3.94	1.13	0.71	3.16	0.023	1765 ± 71	0.3972 ± 0.004	0.3429 ± 0.004	0.09 ± 0.01	0.12
B2-25-FW1	*0.23*	*3.71*	*3.93*	*2.58*	*1.30*	*3.33*		*447*	*0.3914*	*0.3337*	*0.42*	*leak*
E4-IPC-DW-2	0.27	1.70	3.02	4.44	2.42	2.32	0.017	298 ± 2	0.3902 ± 0.002	0.3312 ± 0.002	0.17 ± 0.01	1.01
E5-46-Bh1	11.73	0.21	21.85	0.48	0.45	4.89	0.035	10816 ± 433	0.3930 ± 0.008	0.3409 ± 0.005	0.11 ± 0.01	0.13
EV522FW-HWD	9.24	0.38	2.28	1.19	0.78	3.42	0.025	832 ± 33	0.3918 ± 0.005	0.3358 ± 0.005	0.14 ± 0.01	0.23
EV818FW-FBH	7.06	0.06	1.77	0.32	0.25	1.49	0.011	2985 ± 119	0.4142 ± 0.016	0.3665 ± 0.014	0.09 ± 0.01	0.03
EV818FW-NEPD	8.02	0.06	2.84	0.49	0.35	1.46	0.011	3438 ± 138	0.4239 ± 0.009	0.3722 ± 0.010	0.07 ± 0.01	0.03
K4-41-FW1b	21.32	0.51	5.89	1.87	1.40	1.48	0.011	1197 ± 48	0.3900 ± 0.002	0.3337 ± 0.003	0.10 ± 0.01	0.30
K4-41-FW-2	14.99	0.29	3.22	0.46	0.28	1.52	0.011	2456 ± 98	0.4274 ± 0.015	0.3889 ± 0.012	0.22 ± 0.01	0.17
KL739FW	11.27	0.03	2.32	0.17	0.13	1.28	0.009	6658 ± 266	0.4734 ± 0.018	0.4547 ± 0.011	0.10 ± 0.01	0.02
K4-41-FW-1	*12.39*	*18.75*	*14.85*	*7.65*	*3.94*	*1.39*		*373*	*0.3878*	*0.3290*	*0.47*	*leak*
W6-38-FW3 #1	*7.28*	*5.82*	*4.58*	*3.54*	*1.58*	*1.37*		*340*	*0.3892*	*0.3309*	*0.43*	*leak*
W6-38-FW3 #2	*8.36*	*31.33*	*18.24*	*14.08*	*5.05*	*1.18*		*363*	*0.3862*	*0.3283*	*0.62*	*leak*
ASW	$4.5 \cdot 10^{-4}$	1.67	3.11	3.98	2.57	136.0	1.000	295.5	0.3879 ± 0.006	0.3294 ± 0.004	0.16	1.00

If not explicitly stated, the measurement uncertainty is 2%. Four samples show unreasonably high excess air components (italic) as identified by a ^{20}Ne/^{36}Ar isotope ratio close to that one of air of 0.55. They are probably affected by air contamination and will not be further discussed. The last column states the degree of ^{20}Ne-saturation normalized to an air saturated water (ASW) at 20°C and 1013mbar ($C_{Ne}/C_{Ne}^0 = 1.0$). Samples with values smaller unity are affected by degassing.

cedure, a ^{36}Cl-dead material, Diamond Crystal® Iodized Table Salt, Cargill Foods, was dissolved in 18-MΩcm^{-1} water and subsequently treated like a sample.

3.3.3. U, Th and K composition of rock samples and porosity

Thirty (30) rock samples were collected in mines and their pore water content was gravimetrically determined by drying at 100°C for a minimum of 24 h. The U, Th and K contents were determined at Princeton University by pulverizing the rocks and dissolving weighed aliquots in a heated mixture of concentrated HF and 50% HCl. The dried residue was then dissolved in heated, concentrated H_2SO_4 and almost completely evaporated before adding 50% HCl. The acidified solution was then diluted 100:1 with distilled water and analysed on an ICP-AES.

4. RESULTS AND DISCUSSION

4.1. General Results

Four different types of water samples were analysed and will be discussed: one tap water, one ground water, one pore water, and 16 fissure water samples. The pore and the fissure waters originate from the ultra deep levels in the mines.

The *ground water sample* taken from the lower parts of the local Mooidraai Dolomite aquifer at 4 shaft, Driefontein mine (E4-IPC-DW-2), is fresh water of meteoric origin. The concentrations of dissolved atmospheric noble gases (^{20}Ne, ^{36}Ar, ^{84}Kr, ^{132}Xe) were evaluated as a recharge temperature (Mazor, 1972; Stute et al., 1992b) using the partial re-equilibration model, with temperature, excess air, and degree of fractionation as free parameters (PR model, Aeschbach-Hertig et al., 1999). This resulted in a noble gas temperature of 17.8 ± 0.5°C at 1750 m a.s.l. (above sea level) and an air excess value of ΔNe = 218%. The ^{40}Ar/^{36}Ar ratio of 298 ± 2 is close to the air ratio of 295.5 and the ^{4}He concentration of $2.7 \cdot 10^{-5}$cm^{3}STPg^{-1} exceeds the concentration of air saturated water (ASW, $4.5 \cdot 10^{-8}$cm^{3}STPg^{-1}) by two and a half orders of magnitude. The ^{3}He/^{4}He ratio of $2.3 \cdot 10^{-8}$ identifies the ^{4}He as radiogenic in origin.

The *pore water sample* BE19BWBhDD13677 from an exploration bore hole at Beatrix mine yields a ^{4}He-concentration of $1.85 \cdot 10^{-2}$ cm^{3}STP g^{-1}, five orders of magnitude greater than ASW water. ^{3}He/^{4}He = $3.34 \cdot 10^{-8}$ clearly identifies the ^{4}He as of radiogenic origin. ^{40}Ar/^{36}Ar = 900 requires a radiogenic ^{40}Ar-contribution of ≈ 67%. ^{4}He/^{40}Ar$_{rad}$ = 26.3 exceeds the crustal average production ratio of 4.9 (Taylor and McLennan, 1985, Table 1).

^{134}Xe/^{132}Xe = 0.3919 ± 0.002 (1σ) and ^{136}Xe/^{132}Xe = 0.3378 ± 0.003 (1σ) exceed the atmospheric ratios of 0.3879 and 0.3294, respectively, and indicate a contribution from spontaneous fission of ^{238}U. The inverse fitting technique was applied to interpret the dissolved atmospheric noble gases (^{20}Ne, ^{40}Ar$_{atmospheric}$, ^{84}Kr, ^{132}Xe) of the pore water sample, with ^{40}Ar$_{atmospheric}$ being the atmospheric ^{40}Ar-component from the measured ^{40}Ar-concentration:

$$^{40}Ar_{atmospheric} = {}^{40}Ar_{meas} \cdot \frac{R_{air}}{R_{sample}} \qquad (4.1)$$

with $R_i = (^{40}Ar/^{36}Ar)_i$. The best fit (59% probability) was achieved with the CE-model (closed system equilibration, ta-1), using temperature and excess air as free parameters (Aeschbach-Hertig et al., 1999). The model results for this pore water sample reveal a noble gas temperature of (22.1 ± 0.7)°C, with ΔNe = 80.6% excess air at elevation of 1750 m a.s.l., the elevation of Beatrix mine.

The results of 12 *fissure water samples* (4 out of 16 sampling containers were leaky, namely B2-25-FW1, K4-41-FW-1, W6-38-FW3 #1, and #2) are comparable in most respects, although

Table 3. Degassing corrected noble gas concentrations.

Sample		$C_{He}/C_{He}°$	$C_{Ne}/C_{Ne}°$	$C_{Ar}/C_{Ar}°$	$C_{Kr}/C_{Kr}°$	$C_{Xe}/C_{Xe}°$	[2]±	$(^4He)_d$	$(^{40}Ar_{rad})_d$	$(^{134}Xe_{fiss})_d$	$(^{136}Xe_{fiss})_d$	$(^4He/^{40}Ar_{rad})_d$	$(^{134}Xe_{fiss}/^4He)_d$	$(^{136}Xe_{fiss}/^4He)_d$	$(^{134}Xe_{fiss}/^{40}Ar_{rad})_d$	$(^{136}Xe_{fiss}/^{40}Ar_{rad})_d$	$(^{136}/Xe_{fiss}/^{134}Xe_{fiss})_d$
		[1]remaining fractions of noble gases					[%]	$[10^{-4}]$	$[10^{-4}]$	$[10^{-11}]$	$[10^{-11}]$		$[10^{-9}]$	$[10^{-9}]$	$[10^{-9}]$	$[10^{-9}]$	
								$cm^3\ g^{-1}$ (STP)									
BE19BWBhDD13677	(air)	1.00	1.00	1.00	1.00	1.00	–	184.8 ± 0.9	7.0 ± 0.5	1.3 ± 0.7	2.5 ± 0.9	26.3 ± 2.0	0.7 ± 0.4	1.4 ± 0.5	18.6 ± 9.5	35.5 ± 12.9	1.9 ± 1.2
BE16FW-GDW #1	diff	0.02	0.05	0.08	0.12	0.15	16.4	319.3 ± 52.4	16.8 ± 2.2	3.0 ± 3.8	3.4 ± 4.4	19.0 ± 4.0	0.9 ± 1.2	1.1 ± 1.4	17.9 ± 22.6	20.0 ± 26.1	1.1 ± 2.0
BE16FW-GDW #3	diff +sol.	0.00	0.05	0.11	0.16	0.20	22.8										
BE23FW-A4RD	diff	0.10	0.17	0.24	0.30	0.33	3.6	129.4 ± 4.7	10.9 ± 1.1	1.4 ± 1.7	1.5 ± 2.2	11.8 ± 1.2	1.1 ± 1.3	1.2 ± 1.7	12.8 ± 15.7	14.0 ± 19.7	1.1 ± 2.0
BE24FW-C17W18 #2	diff	0.03	0.06	0.10	0.15	0.18	5.5	141.9 ± 7.8	12.7 ± 1.6	2.0 ± 1.5	1.7 ± 2.3	11.2 ± 1.5	1.4 ± 1.0	1.2 ± 1.6	15.8 ± 11.8	13.5 ± 18.4	0.9 ± 1.3
BE325FW-CTS	diff	0.03	0.06	0.10	0.14	0.17	15.3	456.9 ± 69.9	30.4 ± 3.6	2.7 ± 3.3	3.0 ± 1.0	15.0 ± 2.9	0.6 ± 0.7	0.7 ± 0.2	9.0 ± 10.8	10.0 ± 3.4	1.1 ± 1.4
BE327FW-CTS	diff	0.06	0.12	0.17	0.22	0.25	10.0	323.2 ± 32.3	19.2 ± 2.0	2.8 ± 1.6	3.5 ± 1.5	16.9 ± 2.4	0.9 ± 0.5	1.1 ± 0.5	14.8 ± 8.5	18.4 ± 7.8	1.2 ± 0.9
B2-25-FW1	leak																
E4-IPC-DW-2	(air)	1.00	1.00	1.00	1.00	1.00	–	0.3 ± 0.0	0.02 ± 0.0			10.9 ± 9.0					
E5-46-Bh1	diff @ 70°C	0.08	0.13	0.17	0.20	0.22	18.9	150.8 ± 28.5	123.7 ± 11.8	0.8 ± 2.2	1.9 ± 1.3	1.2 ± 0.3	0.5 ± 1.5	1.3 ± 0.9	0.7 ± 1.8	1.6 ± 1.1	2.4 ± 6.6
EV522FW-HWD	diff	0.14	0.23	0.30	0.35	0.39	11.7	64.0 ± 7.5	4.9 ± 0.5	0.7 ± 1.4	1.0 ± 1.3	13.1 ± 2.0	1.1 ± 2.2	1.6 ± 2.0	14.1 ± 28.6	20.8 ± 25.8	1.5 ± 3.5
EV818FW-FBH	diff	0.01	0.03	0.06	0.09	0.11	4.4	568.7 ± 25.0	26.7 ± 3.6	7.3 ± 5.1	8.9 ± 4.0	21.3 ± 3.0	1.3 ± 0.9	1.6 ± 0.7	27.3 ± 19.5	33.3 ± 15.8	1.2 ± 1.0
EV818FW-NEPD	diff	0.01	0.04	0.06	0.09	0.11	11.6	606.6 ± 70.4	41.9 ± 5.5	14.4 ± 4.3	14.7 ± 4.3	14.5 ± 2.5	2.4 ± 0.8	2.4 ± 0.8	34.4 ± 11.3	35.0 ± 11.3	1.0 ± 0.4
K4-41-FW1b	diff +sol.	0.21	0.30	0.44	0.50	0.55	3.3	99.2 ± 3.3	10.0 ± 0.8	0.4 ± 0.7	0.9 ± 1.0	10.0 ± 0.9	0.4 ± 0.7	0.9 ± 1.0	4.3 ± 7.1	9.0 ± 9.6	2.1 ± 4.0
K4-41-FW-2	diff (air)	*0.02*	*0.05*	*0.08*	*0.11*	*0.13*	*15.7*	681.1 ± 106.9	34.7 ± 4.3	10.5 ± 4.7	14.0 ± 3.8	19.7 ± 3.9	1.5 ± 0.7	2.1 ± 0.6	30.4 ± 14.0	40.5 ± 12.2	1.3 ± 0.7
KL739FW	diff	0.01	0.02	0.04	0.06	0.07	15.1	1548.9 ± 233.9	57.2 ± 8.4	21.2 ± 5.7	27.5 ± 4.9	27.1 ± 5.7	1.4 ± 0.4	1.8 ± 0.4	37.1 ± 11.4	48.0 ± 11.1	1.3 ± 0.4
K4-41-FW-1	leak																
W6-38-FW3 #1	leak																
W6-38-FW3 #2	leak																
Theoretical production ratios for average crustal composition												4.9	1.9	2.3	8.9	10.7	1.2
Average measured results and standard deviation												15.9 ± 6.7	1.1 ± 0.5	1.4 ± 0.5	18.2 ± 10.7	23.0 ± 13.5	1.4 ± 0.4

[1] Model-results: degree of saturation $C_i/C_{i°}$ (normalized to ASW at 20°C and 1013mbar);

[2] mean model offset; index d = corrected for degassing. The applied correction accounts for the under saturation due to diffusive degassing since mining activity and during sampling. For K441FW1b solubility equilibrium with a gas phase is additionally considered: $V_g/V_1 = 0.002$.

Table 4. Fractionation corrected noble gas isotope ratios and concentrations.

Sample	$(^3He/^4He)_f$	$R_{mess}-R_f$	$(^{40}Ar/^{36}Ar)_f$	$(^{134}Xe/^{132}Xe)_f$	$(^{136}Xe/^{132}Xe)_f$	meas. uncert	$(^{40}Ar_{rad})_f$	$(^{134}Xe_{fiss})_f$	$(^{136}Xe_{fiss})_f$	T_s	T_e
	$[10^{-8}] \pm 5\%$	[%]			$R_f \pm \Delta R_{mess}$	Δ_{offset} [%]	$[10^{-4}]$	$[10^{-11}]$	$[10^{-11}]$		
										°C	°C
BE19BWBhDD13677	3.34 ± 0.17	0.0	900 ± 36	0.3919 ± 0.0020	0.3378 ± 0.0030	35.6	7.03 ± 0.50	1.31 ± 0.66	2.50 ± 0.89	33	ΔNe = 80.5%
BE16FW-GDW #1	4.78 ± 0.24	25.7	1305 ± 103	0.3935 ± 0.0070	0.3364 ± 0.0090	128.4	1.40 ± 0.18	0.45 ± 0.56	0.50 ± 0.65	34	34
BE16FW-GDW #3											
BE23FW-A4RD	3.90 ± 0.20	15.8	1244 ± 70	0.3920 ± 0.0050	0.3344 ± 0.0070	140.9	2.61 ± 0.24	0.47 ± 0.57	0.51 ± 0.72	34	34
BE24FW-C17W18 #2	4.01 ± 0.20	23.9	1293 ± 96	0.3933 ± 0.0040	0.3346 ± 0.0070	135.8	1.30 ± 0.16	0.35 ± 0.26	0.30 ± 0.41	33	33
BE325FW-CTS	3.37 ± 0.17	23.5	2177 ± 161	0.3938 ± 0.0070	0.3367 ± 0.0020	27.6	3.13 ± 0.36	0.47 ± 0.56	0.52 ± 0.14	39	39
BE327FW-CTS	3.89 ± 0.19	18.8	1685 ± 106	0.3951 ± 0.0040	0.3394 ± 0.0040	40.0	3.25 ± 0.32	0.71 ± 0.39	0.89 ± 0.35	40	40
B2-25-FW1										35	
E4-IPC-DW-2	2.32 ± 0.12	0.0	298 ± 2	0.3902 ± 0.0020	0.3312 ± 0.0020	112.7	0.02 ± 0.02			25	ΔNe = 218%
E5-46-Bh1	5.91 ± 0.30	17.3	10331 ± 649	0.3909 ± 0.0080	0.3372 ± 0.0050	64.3	21.22 ± 1.91	0.18 ± 0.50	0.43 ± 0.28	37	37
EV522FW-HWD	3.95 ± 0.20	13.4	806 ± 42	0.3904 ± 0.0050	0.3335 ± 0.0050	123.1	1.44 ± 0.14	0.27 ± 0.54	0.40 ± 0.49	37	37
EV818FW-FBH	2.07 ± 0.10	27.9	2773 ± 243	0.4107 ± 0.0160	0.3605 ± 0.0140	45.1	1.58 ± 0.21	0.78 ± 0.55	0.95 ± 0.43	45	45
EV818FW-NEPD	2.02 ± 0.10	27.6	3198 ± 277	0.4204 ± 0.0090	0.3661 ± 0.0100	27.2	2.57 ± 0.33	1.59 ± 0.44	1.61 ± 0.44	45	45
K4-41-FW1b	1.65 ± 0.08	10.8	1172 ± 54	0.3891 ± 0.0020	0.3322 ± 0.0030	106.1	4.41 ± 0.34	0.24 ± 0.39	0.49 ± 0.52	58	58
K4-41-FW-2	2.03 ± 0.10	24.8	2301 ± 184	0.4241 ± 0.0150	0.3830 ± 0.0120	22.4	2.81 ± 0.34	1.38 ± 0.57	1.84 ± 0.41	52	52
KL739FW	1.85 ± 0.09	30.7	6118 ± 603	0.4687 ± 0.0180	0.4459 ± 0.0110	9.4	2.20 ± 0.31	1.51 ± 0.34	1.95 ± 0.18	54	54
K4-41-FW-1										60	
W6-38-FW3 #1										45	
W6-38-FW3 #2										45	
ASW	136		295.5	0.3879	0.3294						

Index f = corrected for fractionation during degassing.

Table 5. Cloride and stable isotopes.

Name of sample	^{36}Cl [10^7] atoms/l	^{36}Cl/Cl [10^{-15}]	Cl^-/L mg/L	δ^{18}O ‰ V-SMOW	δD ‰ V-SMOW
BE16FW-IDW	84.3	34 ± 4	1.458	−5.49	−40.1
BE16FW-GDW #1	65.7	32 ± 4	1.206	−5.85	−42.3
BE23FW-A4RD	52.5	25 ± 5	1.235	−6.17	−41.0
BE24FW-C17W18 #2	82.5	35 ± 4	1.385	−6.13	−42.7
BE325FW-CTS	66.2	27 ± 3	1.435	−6.71	−43.2
BE327FW-CTS	101.5	37 ± 10	1.612	−6.66	−41.2
B2-25-FW1	59.5	27 ± 8	1.295	1.92	−36.9
E4-IPC-DW-2	5.5	209 ± 9	16		
E5-46-Bh1	346.0	9 ± 9	22.600	−13.14	−24.4
EV522FW-HWD	33.0	11 ± 5	1.765	−5.63	−27.7
EV818FW-FBH				−10.87	−36.9
EV818FW-NEPD	55.3	12 ± 3	2.730	−10.24	−35.9
KL739FW				−7.24	−20.4
K4-41-FW-1	13.9	4 ± 4	1.898	−5.71	−27.7
WDF2b	8.7	8 ± 9	639	−6.58	–
EV811FW-1XCA	24.5	24 ± 5	600	−5.02	−30.0
E5-46-sump	7.6	3 ± 6	1.789	−0.15	–
tap water. #2 shaft	9.6	704 ± 14	8		
calcul. atmos. Input	0.01	420 ± 200	0.01		
line blank		0 ± 4	1.000		

they were sampled at four different gold mines from all over the basin and cover a wide depth range (Table A1). Unlike the ground and pore water samples, the noble gas abundance pattern of the fissure water samples showed significant undersaturation relative to solubility equilibrium with air. This undersaturation ranges between 70 to 98% for Neon normalized to air saturated water (ASW) at 20°C at 1013 mbar (see Table 2, $C_{Ne}/C_{Ne}°$). Processes causing this undersaturation and affecting elemental and isotopic noble gas composition will be discussed in detail in sections 4.4.2 to 4.4.4.

Measured ^{4}He-concentrations ($(3.6–21) \cdot 10^{-4}$ cm^{3}STP g^{-1}) of the fissure waters are high and range over less than one order of magnitude. $^3He/^4He = (1.3–4.9) \cdot 10^{-8}$ identifies the ^{4}He as radiogenic in origin. The $^{134}Xe/^{132}Xe$ and $^{136}Xe/^{132}Xe$-ratios are higher compared to air values of 0.3879 and 0.3294, respectively. Most Xe-ratios range between 0.390 and 0.398 for $^{134}Xe/^{132}Xe$ and 0.330 and 0.343 for $^{136}Xe/^{132}Xe$, respectively, with four exceptions (EV818FW-FBH, EV818FW-NEPD, KL739FW, and K4-41-FW-2) where values are between 0.410 and 0.473 for $^{134}Xe/^{132}Xe$ and between 0.366 and 0.455 for $^{136}Xe/^{132}Xe$ (Table 2). The $^{136}Xe_{fiss}/^{134}Xe_{fiss}$-ratios with an average of 1.4 ± 0.4 (Table 3) identify $^{134}Xe_{fiss}$ and $^{136}Xe_{fiss}$ as due to spontaneous fission of ^{238}U as their theoretical production ratio is 1.2 (Shukoljukov et al., 1974). The $^{40}Ar/^{36}Ar$ ratios of all mine water samples were very high (Table 4, 806 to 10331).

4.2. ^{36}Cl-Ratios and ^{36}Cl-Concentrations

The atmospheric (hypogene) ^{36}Cl/Cl-input ratio for southern Africa of $(420 \pm 200) \cdot 10^{-15}$ is calculated from a proposed value for natural, atmospheric ^{36}Cl fallout at 27 ° S (South Africa) of (12–18) atoms ^{36}Cl m^{-2}s^{-1} (Lal and Peters, 1967), a mean annual precipitation of (688 ± 20)mm yr^{-1} (IAEA/WMO, 2002): GNIP database for Pretoria, 27-yr long, monthly record), and Cl concentrations in precipitation of (0.1 ± 0.05) mg Cl l^{-1}. This calculated meteoric input is equivalent to a ^{36}Cl-concentration of $0.01 \cdot 10^7$ atoms l^{-1}. This should be regarded only as crude estimate for the initial ^{36}Cl/Cl-ratio or ^{36}Cl-concentration. First, because the sea spray contribution to Cl decreases exponentially with the distance from the coast (Bentley et al., 1986). And secondly, because additional ^{36}Cl produced near the surface may be released by weathering (epigene ^{36}Cl) into the water cycle. Therefore, we measured the ^{36}Cl/Cl-ratio in local ground water: ground water from the base of the local dolomite aquifer (E4-IPC-DW-2) and tap water from #2 shaft at Beatrix gold mine (public water supply, most likely from the top of the local dolomite aquifer) were sampled. The measured ^{36}Cl/Cl ratio of the tap water is the highest of the data set with $(704 \pm 14) \cdot 10^{-15}$ (Table 5). The ^{36}Cl/Cl ratio of the ground water sample is $(204 \pm 9) \cdot 10^{-15}$(E4-IPC-DW-2). The estimated atmospheric input ratio agrees within 2σ with the measured ratios of the tap water and the ground water sample.

All fissure water samples have significantly lower ^{36}Cl/Cl ratios and range between $4 \cdot 10^{-15}$ and $(37 \pm 9) \cdot 10^{-15}$ (overall ^{36}Cl/Cl blank is $(0 \pm 4) \cdot 10^{-15}$). To identify the source of the ^{36}Cl, the ^{36}Cl/Cl ratio is plotted versus the ^{36}Cl-concentration of all water samples (Fig. 2a). The tap water sample is considered to best represent the ^{36}Cl/Cl-input ratio and input ^{36}Cl-concentration of the atmospheric fallout of ^{36}Cl. If the atmosphere were the only source of ^{36}Cl, the results of all other water samples should plot along a straight line between the tap water sample and the origin of the plot as a result of ^{36}Cl decay (Fig. 2a). Only the dolomite ground water sample is interpreted to be the result of ^{36}Cl-decay of atmospheric input and/or addition of dead Cl to surface (tap) water.

In contrast, all fissure water samples plot significantly off the decay line between the tap water and the origin of the plot and have higher ^{36}Cl-concentrations than surface water with about $10 \cdot 10^7$ atoms ^{36}Cl l^{-1} (tap water, Beatrix #2 shaft). The

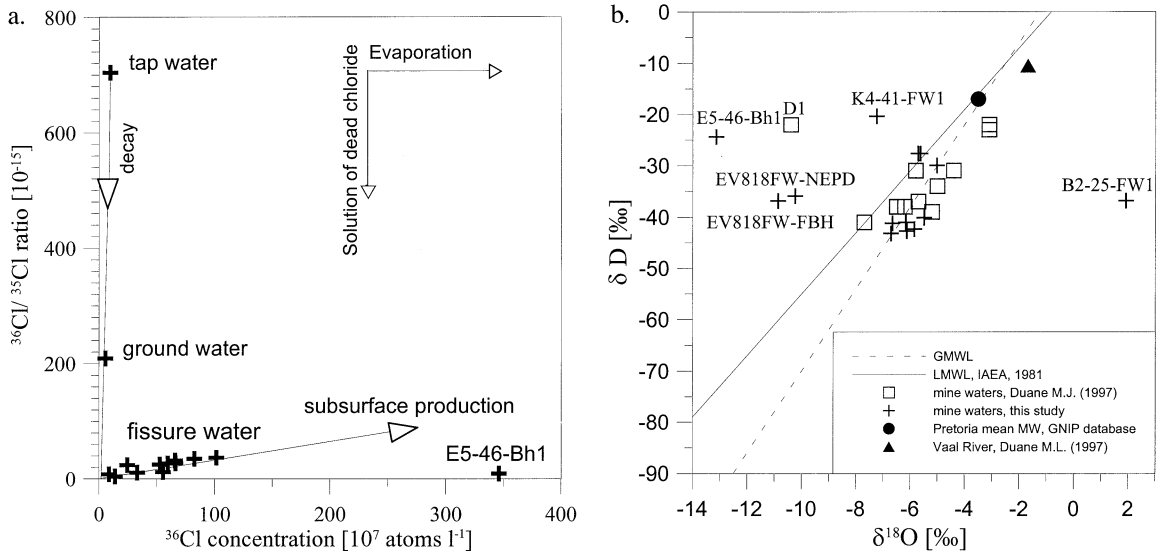

Fig. 2. **a:** Ratios of ^{36}Cl/Cl versus ^{36}Cl concentrations. The high ^{36}Cl/Cl ratios of the tap water and the ground water (E4-IPC-DW-2) are due to atmospheric input. The low ^{36}Cl/Cl ratios and high ^{36}Cl concentrations of the fissure water samples are due to subsurface production (inclining arrow at bottom of figure). **b:** δD versus δ^{18}O. Results of this study (cross symbol) are compared with results from Duane et al. (1997): mine water (rectangle), Vaal River water (triangle); the Global (GMWL, Craig, 1961) and Local (LMWL) Meteoric Water Lines (Mazor and Verhagen, 1983), and mean precipitation from Pretoria, SA, derived from a 27-yr, monthly record (filled circle) (IAEA/WMO, 2002).

measured high ^{36}Cl-concentrations of the fissure waters (7.6 to 346) $\cdot 10^7$atoms^{36}Cl l^{-1} exclude the atmosphere as the source of this ^{36}Cl. Thus, subsurface production (secondary neutron capture by ^{35}Cl; Bentley et al., 1986; Andrews et al., 1989) is the source for ^{36}Cl and dominates the ^{36}Cl budget in the fissure water samples. But the observed ^{36}Cl and Cl signatures are still ambiguous: The high ^{36}Cl-concentrations could originate from dissolved Cl with a ^{36}Cl/Cl-ratio close to secular equilibrium. Then the data would not tell much about the age of the water. Only if substantial dissolution of subsurface Cl can be excluded, then high ^{36}Cl-concentrations substantiate that the bulk of all fissure water samples are older than 1.5 Ma, 4–5 times the half-live of ^{36}Cl of 301 kyr. Although the occurrence of evaporites in the Witwatersrand Basin is not documented, a final decision will only be made after comparison with calculated model ages derived from the nucleogenic noble gas signatures in section 4.4.9.

The secular equilibrium ratio R_{se} was calculated for sample E5-46-Bh1 according to Bentley et al. (1986, Eqn. 6) and yielded a $R_{se} \cong 11 \cdot 10^{-15}$ compared to the measured value of $9 \pm 9 \cdot 10^{-15}$, equivalent to a ^{36}Cl-concentration of $346 \cdot 10^7$ atoms l^{-1} (Table 5). The high uncertainty of this particular result is caused by interference with ^{36}S.

These calculations for R_{se} are based on the mineral composition of the Klipriviersberg Lava (Antrobus et al., 1986, p.573, Table 3), U and Th concentrations of 4 and 10 ppm, a porosity of n = 0.01%, a neutron flux Φ_n of ~8 n $kg^{-1}yr^{-1}$, a decay constant λ_{36} of ^{36}Cl of $2.3 \cdot 10^{-6}$ yr^{-1} and a Cl concentration of 22.4 g l^{-1}. In doing so, we ignore the results of our own analysis of the U concentration for the Klipriviersberg Lava (Table 1). Thus, we do not consider our value of 419 ppm to be representative for the average host rock formation.

4.3. Stable Isotopes δD and δ^{18}O

The δD and δ^{18}O of most fissure water samples fall on or close to the meteoric water line. However, as they are more depleted in δD and δ^{18}O than present local mean annual precipitation, the Vaal river, and the dolomite ground water (Fig. 2b), the fissure water most likely infiltrated at either higher elevations or during a time when the mean annual temperature was cooler than today. Noble gas temperatures can not constrain these two options, as the significant degassing of the fissure water samples obliterated this sensitive palaeotemperature information effectively. Sample B2-25-FW1, to the right of the GMWL, is most likely affected by isotope exchange with the surrounding rock that enriches the pore water in δ^{18}O.

Of special interest are the two samples E5-46-Bh1 and D1 (Duane et al., 1997) that lie to the left of the meteoric water line (Fig. 2b). Both are saline fissure water samples from the Ventersdorp Supergroup, D1 from the Mpening mine, which is proximal to E5-46-Bh1 from the Driefontein mine. Such depleted δ^{18}O values indicate water-rock interaction by alteration of silicates to clay minerals coupled with a low water-rock ratio.

D1 also has the highest ^{87}Sr/^{86}Sr ratio in the data set presented by Duane et al. (1997), and E5-46-Bh1 yields the highest ^{40}Ar/^{36}Ar (>10 000) in this study. For sample D1, the relatively high ^{87}Sr/^{86}Sr-value indicates release of radiogenic ^{87}Sr from the mineral phase into the fluid phase (Duane et al., 1997). Similarly, ^{40}Ar/^{36}Ar of E5-46-Bh1 implies the release of significant amounts of radiogenic ^{40}Ar from the mineral phase and its accumulation in the fluid. The significantly higher salinity of these two samples is consistent with hydrologic isolation from the other fissure waters (see also 4.10).

These factors indicate that two different types of deep sub-

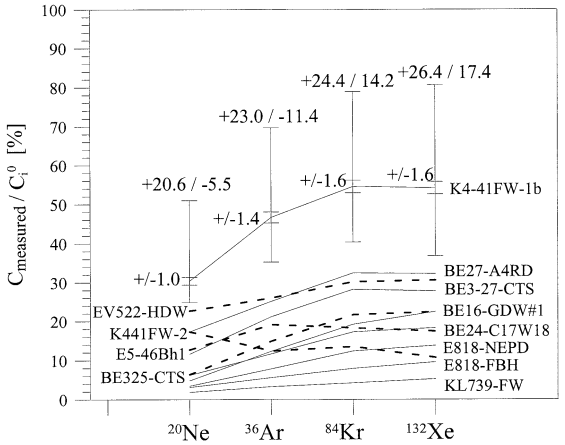

Fig. 3. Measured atmospheric noble gas concentrations C_i (i = ^{20}Ne, ^{36}Ar, ^{84}Kr and ^{132}Xe) of the fissure water samples, normalized to air saturated water C_i^0 (ASW, 20°C and 1013 mbar). C_i/C_i^0 expresses the fraction of ASW present in the samples. For all fissure water samples C_i/C_i^0 is smaller than 100%. The labels on the left side refer to the dashed lines, those on the right to the solid lines. Error bars are shown exemplarily only for one sample, but valid for all samples. Measurement uncertainty for C_i/C_i^0 ranges from 1.0% to 1.6% and is minor compared to the significant uncertainty arising from a variation of ±5°C and +20/−200 mbar for the equilibration conditions of ASW. The combined uncertainty of the initial atmospheric noble gas concentrations C_i^0 and of the measurement uncertainty is considerable, ranging from (+20.6/−5.5) % to (+26.4/−17.4) % for C_i/C_i^0.

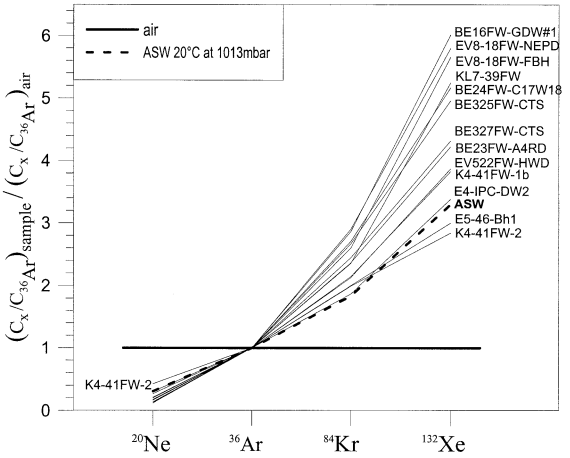

Fig. 4. Measured noble gas concentrations of fissure water samples divided by their ^{36}Ar concentrations, and normalized to the respective air ratio (x_i/^{36}Ar)sample/(x_i/^{36}Ar)air, with x_i = ^{20}Ne, ^{36}Ar, ^{84}Kr, ^{132}Xe. All samples show an elemental fractionation pattern relative to ASW: The ^{20}Ne/^{36}Ar-ratio is smaller—in comparison to ASW—and the ^{84}Kr/^{36}Ar- and the ^{132}Xe/^{36}Ar-ratio is larger—in comparison to ASW. This elemental separation pattern is due to the processes causing the undersaturation: diffusive gas loss in non-equilibrium and/or equilibration with a non-atmospheric gas-phase.

surface water may exist in the Witwatersrand Basin. First, moderately saline fissure water is widely dispersed over the Witwatersrand Basin in various depths. It is the most abundant type and is interpreted as originating from an extended network of water-bearing fractures, always associated with faults and dykes; with long residence times in the subsurface and migrating along extended pathways. Second, there exists highly saline fissure water distinctively enriched in radiogenic isotopes and significantly affected by water rock interaction. This second type of fissure water is interpreted as originating from hydrologically isolated water and gas pockets, analogous to huge fluid inclusions. If it ever was of meteoric origin, it has lost its characteristic isotopic signature due to water-rock interactions.

4.4. Noble Gas Data

4.4.1. Undersaturated fissure water samples

A striking characteristic of the fissure water samples is their undersaturation with respect to dissolved atmospheric noble gases. To illustrate the degree of undersaturation, the measured noble gas concentrations are compared to those of air saturated water (ASW). Figure 3 shows these relative noble gas concentrations C_i/C_i^0, where *i* stands for ^{20}Ne, ^{36}Ar, ^{84}Kr and ^{132}Xe. ASW at 20°C, 1013 mbar, no excess air and zero salinity is chosen arbitrarily (equilibration conditions are not known, but should fall into a rage of (20 ± 5)°C and (1013 + 20/−200) mbar). The resulting uncertainties of the *relative* noble gas concentrations C_i/C_i^0 are significant (ranging from (+20.6/−5.5) % to +26.4/−17.4) %) and exceed the analytical uncertainties of ±1.0% to ±1.6%. The pore water and the ground water sample are not under saturated ($C_i/C_i^0 \approx 100\%$, Table 2) and are therefore not displayed in Figure 3.

Assuming the mine waters were once equilibrated with atmospheric noble gases during the recharge process, two processes can cause the observed undersaturation of the atmospheric noble gases: (1) diffusive degassing in a non-equilibrium state, and (2) equilibration of the water with a non-atmospheric gas phase, e.g., CH_4, and H_2, etc. These two processes are discussed in more detail below. In section 4.4.4. the maximum isotopic fractionation associated with diffusive degassing is quantified to ascertain whether the elevated ^{40}Ar/^{36}Ar- and $^{134(136)}$Xe/^{132}Xe-isotope ratios are the result of fractionation during the diffusive degassing or the result of radiogenic and fissiogenic enrichment. This is essential to the interpretation of the isotopic ratios and the subsequent calculation of model ages.

4.4.2. Elemental fractionation accompanying undersaturation

The undersaturation of the fissure waters is accompanied by elemental fractionation. To illustrate this the ratios of the measured concentrations of ^{20}Ne, ^{36}Ar, ^{84}Kr and ^{132}Xe relative to the ^{36}Ar concentration are normalized to the corresponding ratios for air (Fig. 4). Water samples (thin lines) should be compared with the thick dashed line that represents water saturated with atmospheric noble gases (ASW at 1013 mbar, 20°C). All fissure water samples exhibit an elemental composition that is not consistent with ASW. The normalized ^{20}Ne/^{36}Ar-ratios are lower than ASW and normalized ^{84}Kr/^{36}Ar- and ^{132}Xe/^{36}Ar-ratios are larger than ASW (for ^{20}Ne/^{36}Ar-ratios see Table 2). The calculated error of the normalized ratios is 3.6−4.3%, reflecting just measurement uncertainty. Only sample (K4-41-FW-2) indicates some ′Ne-excess’, which we attribute to mine air entrapped in the sampling container during

sampling. The Kr signal of E5-46-Bh1 was affected by discrimination during measurement by the extremely high radiogenic ^{40}Ar-concentrations and will not be included in this discussion.

4.4.3. Conceptual model explains degassing

We apply a conceptual model to the noble gas data of the fissure water samples to explain the undersaturation of the atmospheric noble gases and the elemental fractionation pattern within the given uncertainties. For an initial ASW that is subject to rapid degassing without reaching equilibrium, the dissolved noble gases are fractionated according to their diffusion coefficients. The diffusion coefficients $D_{i(T)}$ of the different noble gas components i = He, Ne, Ar, Kr and Xe are temperature dependent (Eyring, 1936):

$$D_i(T) = A \cdot e^{\left(\frac{-E_a}{RT}\right)} \; [10^{-5}\ \mathrm{cm^2/s}] \qquad (4.2)$$

with R the universal gas constant of 8.3143J K^{-1} mol^{-1}, T the temperature of the water during the degassing process [K] (for the sampling temperature T_s see Table 4, for values $D_{i(T)}$ see Table A2 in the appendix). The parameter A and the activation energy for diffusion in water E_a were derived from experimental results covering the temperature range between 5 and 35°C (Jähne et al., 1987). As the sampling temperature exceeds this range, we consider an uncertainty of 3% instead of the reported 1%. The degree of undersaturation of one noble gas component $C_i/C_i°$ is proportional to the degree of undersaturation of another noble gas—in this case Ne in ASW at 20°C and 1013 mbar—and depends on the ratio of the diffusion coefficients $D_{i(Ts)}$ of these two gas components, i and Ne:

$$\frac{C_i}{C_i^0} = \left(\frac{C_{Ne}}{C_{Ne}^0}\right)^{\sqrt{\frac{D_i(T_1)}{D_{Ne}(T_2)}}} \qquad (4.3)$$

with i = ^{36}Ar, ^{84}Kr or ^{132}Xe (Zartman et al., 1961; Stute et al., 1992b).

In a second scenario, we consider the total observed loss of gas into a gas phase consisting of only non-atmospheric gases, such as CH_4. Here the degree of undersaturation $C_i/C_i°$ depends on the volume ratio of the gas phase to the liquid phase V_g/V_l at STP (**s**tandard **t**emperature and **p**ressure, 20°C, 1013 mbar) and the solubility $b_{i(T)}$ of each gas component (Zartman et al., 1961; Stute, 1989):

$$\frac{C_i}{C_i^0} = \frac{1}{\left(1 + \frac{1}{\beta_i(T)} \cdot \frac{T^0}{T_s} \cdot \frac{V_g}{V_l}\right)} \qquad (4.4)$$

with T_s the sampling temperature and T^o = 273.15 K. The concentration of the dissolved gases in the liquid is in equilibrium with this headspace concentration C_{gi} according to Henry's Law:

$$C_i = \beta_i(T) \cdot \frac{C_{gi}}{\rho} \qquad (4.5)$$

where ρ is the density of the water and C_{gi} the concentration of the gas component i in the head space in volume fraction [STP]. Looking at the relative depletion of one element compared to a reference, $C_{Ne}/C_{Ne°}$, the degree of undersaturation of anynoble gas component i relative to that of Ne is

$$\frac{C_i}{C_i^0} = \frac{1}{1 + \frac{\beta_{Ne}(T)}{\beta_i(T)} \cdot \left(\frac{C_{Ne}^0}{C_{Ne}} - 1\right)} \qquad (4.6)$$

with i = ^{36}Ar, ^{84}Kr or ^{132}Xe.

The temperature dependent solubilities $\beta_{i(T)}$ of Crovetto et al. (1982) for the range between 30 and 330°C were used in Eqn. 4.6. The authors state the overall precision in Henry's Law constants is 1–2%.

Pressure release and dewatering might have enabled a gas phase to develop into which the dissolved gases could exsolve. This scenario has been discussed in detail by Andrews and Wilson (1987). The elemental separation pattern caused by this solubility equilibrium with an open gas phase is more pronounced in comparison to the diffusive process at the same temperature T_s (Fig. 5), compare the steeper dashed line 'b' with line 'a').

Using the measured C_{Ne}/C_{Ne}^o values in Eqn. 4.3 and Eqn. 4.6, and T = T_s, the relative concentrations $C_iC_i^o$ can be calculated for i = ^{36}Ar, ^{84}Kr, and ^{132}Xe for both scenarios—diffusive degassing and solubility equilibrium. (For sample K4-41-FW-2 the air-excess has a four times larger effect on C_{Ne}/C_{Ne}^o than on $C_{36Ar}/C_{36_{Ar}}^o$. Therefore, here the relative Ar concentration is used in instead of the relative Ne concentration in Eqn. 4.3 and 4.6.). For 10 samples (BE16FW-GDW#1, BE23FW-A4RD, BE24FW-C17W18 #2, BE325FW-CTS, BE327FW-CTS, EV818FW-FBH, EV818FW-NEPD, EV522FW-HWD, KL739FW and E4-46-Bh1) the diffusive degassing scenario explains the measured data within the uncertainties stated for C_i/C_i°, and better explains the fractionation pattern than the

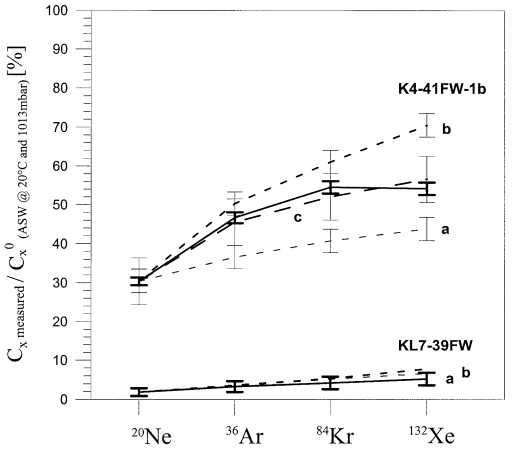

Fig. 5. Data (solid lines) and model results (dashed lines) of two selected samples: For KL7-39FW the amount of undersaturation and the elemental separation pattern can be explained within the stated uncertainties of $C_i/C_i°$ by both scenarios: (a) diffusive degassing at sampling temperature and (b) solubility equilibrium with a non-atmospheric gas phase. For the majority of samples, only scenario (a) fits or fits significantly better than scenario (b). For three samples, neither scenario fits the data within the uncertainty of $C_i/C_i°$, and a combination of (a) and (b) → (c) is used to explain undersaturation and fractionation. For K4-41-FW-1b, 55% of the observed loss of Ne was lost due to (a) and, 15% was due to (b).

equilibration model. For sample K4-41-FW-1b, we consider a combination of diffusive degassing and equilibrium with a gas phase as the most likely scenario, as only then can the model explain the data within the uncertainty given for C_i/C_i^0 (see dashed line "c" in Fig. 5).

For sample BE16FW-GDW #3 the calculated elemental separation pattern is depleted compared to the observed pattern. Here, the model fit—the mean deviation between modeled and measured relative concentration—exceeds 20%, whatever scenario or combination of scenarios we choose. Therefore, we do not consider this sample in the following discussions (see "mean model offset" in Table 3).

Mean model offset

$$= \left(\frac{1}{3} \sum_{i=Ar,Kr,Xe} \sqrt{[(C_i/C_i^0)_{\text{model}} - (C_i/C_i^0)_{measured}]^2} \right) \Big/ (C_{Xe}/C_{Xe}^0)_{measured} \quad (4.6A)$$

Generally, we conclude the undersaturation is due to rapid degassing in non-equilibrium. For on exception—sample K4-41-FW1b—the model best fits the observed fractionation patterns when the loss due to diffusion controlled degassing amounts to 55% and a loss due to solubility equilibrium degassing with an open gas phase of another 15%; corresponding with a volume ratio $V_g/V_l = 0.002$. Note that the equilibration model is quite sensitive to variations in V_g/V_l. At a sampling temperature of 58°C, the mean deviation between the modeled and the measured relative concentrations amounts to only 3.3%. The model results C_i/C_i^0 for $i = {}^4He_{atmospheric}$, ^{20}Ne, ^{36}Ar, ^{84}Kr and ^{132}Xe are given in Table 3.

Based on these model results, the concentrations of ^4He, ^{20}Ne, ^{40}Ar, and ^{132}Xe are corrected for degassing losses. The corrected nucleogenic isotope concentrations of ^4He, $^{21}Ne_{nucl}$, $^{40}Ar_{rad}$, $^{134}Xe_{fiss}$ and $^{136}Xe_{fiss}$ are listed in Table 3 and marked with index 'd' (corrected for *d*egassing).

For sample E5-46-Bh1 the model results were improved significantly by considering a degassing temperature (T = 70°C) that is significantly higher than T_s (37°C). For a detailed discussion on that sample see 4.10.

Generally, we conclude the undersaturation is due to rapid degassing in non-equilibrium. However, given the important uncertainties of the assumptions for the equilibration conditions, also the corrected concentrations that result from this model have important uncertainties. More relevant, the models quantitatively explain the undersaturation and enable an evaluation of the impact of the process on the isotopic ratios.

4.4.4. Isotopic fractionation

To derive residence times from isotopic ratios - in particular from $^{40}Ar/^{36}Ar$ and $^{134(136)}Xe/^{132}Xe$—the effect of non-equilibrium degassing on the isotopic fractionation must be considered. Jähne et al. (1987) studied the isotopic fractionation in the diffusion coefficient and interpreted them as proportional to the inverse of the square root of the *reduced mass*: $D \propto 1/\sqrt{m^*}$. The reduced mass m* of the isotope of interest is

$$m_i^* = \frac{m_i \cdot m_x}{m_i + m_x} \quad (4.7)$$

with m_x the mass of the medium of the boundary layer (Marty, 1984).

We consider the diffusion coefficients in the water to control the flux of noble gas atoms across the air-water interface. And because of the hydrogen bonds in the liquid phase, the effective mass is not 18 (mass of H_2O), but far larger. Therefore, in the limit $x \rightarrow \propto$ Eqn. 4.7 becomes $m_i^* = m_i$. In fact, the experimental results from Jähne et al. (1987) do agree within the uncertainty with both scenarios, with $m_x = 18$ as well with $m_i^* = m_i$ in the limit $x \rightarrow \propto$.

This isotopic fractionation provoked by non-equilibrium degassing is summarized in the following equation, for example for the ^{134}Xe-^{132}Xe-isotope fractionation:

$$F_{^{134}Xe/^{132}Xe} = \frac{^{134}Xe/^{132}Xe}{^{134}Xe^0/^{132}Xe^0} = \frac{^{134}Xe/^{134}Xe^0}{^{132}Xe/^{132}Xe^0}$$

with $^{132}Xe/^{132}Xe^0 = C_{132_{Xe}}/C_{132_{Xe}^0}$ and

$$^{134}Xe/^{134}Xe^0 = (C_{132_{Xe}}/C_{132_{Xe^0}}) \sqrt{D_{134}(T)/D_{132}(T)} \quad (4.8)$$

(see eq. 4.3) and $m_i^* = m_i$

$$F_{^{134}Xe/^{132}Xe} = (C_{132_{Xe}}/C_{132_{Xe^0}}) \sqrt{\sqrt{(m_{132}/m_{134})} - 1}$$

The index 0 refers again to the concentration of ASW at 20°C and 1013 mbar. The isotope fractionation increases with the relative difference of the mass and the degree of degassing.

Isotopic fractionation caused by diffusion is largest for $^3He/^4He$ and is 10–30% of the measured ratio or 2–6 the measurement uncertainty of the ratio. Still, the correction of the isotope ratio has no effect on the calculated ^4He-model age as the overall shift from air ratio is so large. For the $^{136}Xe/^{132}Xe$-ratio, on the other hand, the calculated elemental fractionation caused by diffusion is the smallest due to the small relative difference of the masses. The correction for isotope fractionation due to degassing amounts to less than 2% of the ratio, about the same as the measurement uncertainty (Table 2). All relevant ratios, $^3He/^4He$, $^{40}Ar/^{36}Ar$, $^{134}Xe/^{132}Xe$ and $^{136}Xe/^{132}Xe$, are corrected for this isotopic fractionation due to degassing in non-equilibrium. The corrected ratios are list listed in Table 4 and marked with the index 'f' (corrected for *f*ractionation due to degassing). These corrected ratios indicate the fissure water isotope ratios are an offset from air ratio due to radiogenic or fissiogenic production and not an artefact due to diffusive degassing during mining and sampling.

4.4.5. Crustal fluxes and accumulation of in-situ produced isotopes

The time required to produce the observed dissolved radiogenic, nucleogenic and fissiogenic noble gas concentrations, C_i, depends on the in-situ accumulation rate A_{is} and the accumulation of a crustal flux, J_i, in the sampling depth h (Torgersen and Clarke, 1985):

$$t = \frac{C_i}{\left(A_{is}(i) + \frac{J_i}{n \cdot h \cdot \rho_w} \right)} \quad (4.9)$$

The in situ accumulation rate in the pore water, A_i, depends on the production rate P_i, the porosity n, the release factor, λ_i, and the rock and water densities ρ_s and ρ_w:

$$A_{is}(i) = \lambda_i \cdot \frac{1-n}{n} \cdot \frac{\rho_s}{\rho_w} \cdot P_i \ (\mathrm{cm^3STPg_{water}^{-1}yr^{-1}}) \tag{4.10}$$

with i = ^{4}He, ^{40}Ar, ^{134}Xe. For calculation of model ages, we use $\lambda_{He} = \lambda_{Ar} = 1$ for the release coefficients of He and Ar. For λ_{Xe}, Ragettli et al. (1994) determined values between 0.023 and 0.112 for median grain sizes between 30 and 250 mm. But we consider this Xe-release coefficient as a model parameter in section 4.4.9 and allow λ_{Xe} to range from 0.1 to 0.5.

The production rate of $^4He_{rad}$, $^{40}Ar_{rad}$, and $^{134(136)}Xe_{fiss}$ (P_4, P_{40}, and $P_{134(136)}$) are proportional to the U-, Th-content [ppm] and K-content [%] of the host rock matrix:

$$P_4 = 1.19 \cdot 10^{-13}\ \mathrm{U} + 2.88 \cdot 10^{-14}\ \mathrm{Th}\ (\mathrm{cm^3STPg_{rock}^{-1}yr^{-1}}) \tag{4.11}$$

$$P_{40} = 3.887 \cdot 10^{-14}\ \mathrm{K}\ (\mathrm{cm^3STPg_{rock}^{-1}yr^{-1}}) \tag{4.12}$$

$$P_{134} = 4.14 \cdot 10^{-22}\ \mathrm{U}\ (\mathrm{cm^3STPg_{rock}^{-1}yr^{-1}}) \tag{4.13}$$

$$P_{136} = 4.98 \cdot 10^{-22}\ \mathrm{U}\ (\mathrm{cm^3STPg_{rock}^{-1}yr^{-1}}) \tag{4.14}$$

(Shukoljukov et al., 1974), with resulting production ratios of $P_4/P_{40} \cong 4.9$ (crustal average, see Table 1) and $P_{136}/P_4 = 2.3 \cdot 10^{-9}$ (Wasserburg and Mazor, 1965). ^{4}He and ^{40}Ar crustal flux values have been derived from various ground water field studies and J_{He} ranges from $2.1 \cdot 10^{-7}$ $\mathrm{cm^3STPcm^{-2}yr^{-1}}$ (Germany, Osenbrück et al., 1998), to $4 \cdot 10^{-7}$ $\mathrm{cm^3STPcm^{-2}yr^{-1}}$ (Hungary, Stute et al., 1992a) to $36 \cdot 10^{-7}$ $\mathrm{cm^3STPcm^{-2}yr^{-1}}$ (Australia, Torgersen and Clarke, 1985). For ^{40}Ar, the crustal flux (J_{40Ar}) estimates range from $(2.5–10.5) \cdot 10^{-7}$ $\mathrm{cm^3STPcm^{-2}yr^{-1}}$ (Wasserburg et al., 1963), to $6.3 \cdot 10^{-7}$ $\mathrm{cm^3STPcm^{-2}\ yr^{-1}}$ (Australia, Torgersen et al., 1989) to $(21–28) \cdot 10^{-7}$ $\mathrm{cm^3STPcm^{-2}yr^{-1}}$ (atmospheric model, Hamano and Ozima, 1978).

^{40}Ar/^{36}Ar values of the fissure water samples are all greater than the atmospheric ratio of R_{air} = 295.5. The radiogenic $^{40}Ar_{rad}$ component is calculated from the ^{40}Ar concentration corrected for degassing $(^{40}Ar_{rad})_d$ and the ^{40}Ar/^{36}Ar ratio of the sample corrected for fractionation $(^{40}Ar/^{36}Ar)_f$, R_{sample}:

$$^{40}Ar_{rad} = \frac{R_{sample} - R_{air}}{R_{sample}} \cdot {}^{40}Ar_d\ (\mathrm{cm^3STPg^{-1}}) \tag{4.15}$$

The fissiogenic Xe was calculated from the $(^{134(136)}Xe/^{132}Xe)_f$ ratios and the concentration derived after correction for degassing $(^{132}Xe_{fiss})_d$ using the relationship

$$^{i}Xe_{fiss} = \frac{{}^{i}R_{fiss}}{({}^{i}R_{fiss} - {}^{i}R_{air})} \cdot ({}^{i}R_{sample} - {}^{i}R_{air}) \cdot {}^{132}Xe_d\ (\mathrm{cm^3STPg^{-1}}) \tag{4.16}$$

where $^iR_{fiss}$ stands for either $^{134}R_{fiss} = P(^{134}Xe/^{132}Xe) = 1.398$ or $^{136}R_{fiss} = P(^{136}Xe/^{132}Xe) = 1.681$; $^iR_{air}$ stands for the air Xe ratio of either $^{134}Xe/^{132}Xe = 0.3879$ or $^{136}Xe/^{132}Xe = 0.3294$ (Ozima and Podosek, 1983). This equation takes into account the ^{134}Xe, ^{136}Xe, and ^{132}Xe production by fission processes.

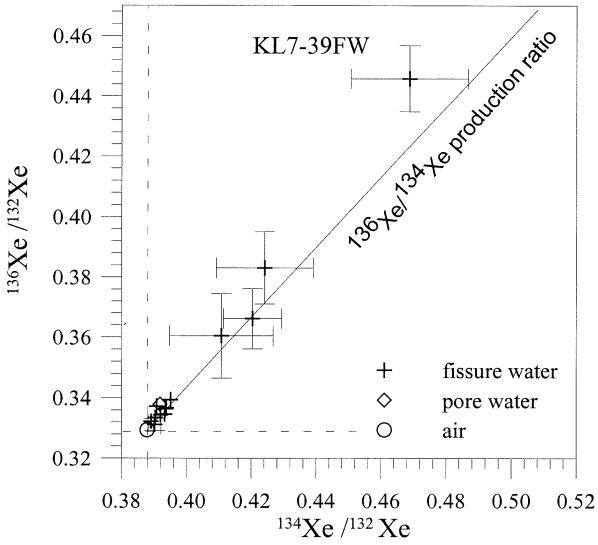

Fig. 6. $^{134}Xe/^{132}Xe$ versus $^{136}Xe/^{132}Xe$ of the all samples. The circle and the vertical and horizontal dashed lines indicate the value for ASW). The solid line indicates the theoretical production ratio P_{136}/P_{134}.

4.4.6. ^{4}Helium and $^{134(136)}$Xenon

The ^{3}He/^{4}He-ratios of all fissure water, pore water and ground water samples clearly identify the ^{4}He to be of radiogenic origin. The average $(^3He/^4He)_f$-ratio is $(3.3 \pm 1.3) \cdot 10^{-8}$. The isotope ratios $(^{134}Xe/^{132}Xe)_f$ and $(^{136}Xe/^{132}Xe)_f$ clearly correlate and fall on the theoretical production line with a slope of 1.2 (Fig. 6). The average fissiogenic isotope ratio of $(^{136}Xe/^{134}Xe)_d = 1.4 \pm 0.4$ (Table 3, bottom line, last column) compares well with the theoretical production ratio $P_{136}/P_{134} = 1.2$ (Shukoljukov et al., 1974).

Furthermore, the average $^{134}Xe_{fiss}/^4He$ and $^{136}Xe_{fiss}/^4He$ values of the fissure water samples $\{(1.1 \pm 0.5) \cdot 10^{-9}$ and $(1.4 \pm 0.5) \cdot 10^{-9}\}$ lie within a factor of <2 of the predicted production ratios of $1.9 \cdot 10^{-9}$ and $2.3 \cdot 10^{-9}$, respectively (Fig. 7a, and Table 3, bottom line). As all three isotopes originate from U, this systematic offset from the production ratio is best explained by different release coefficients for He and Xe: λ_{Xe} must be in the order of 0.5.

4.4.7. ^{40}Argon and its ratios with $^{134(136)}$Xenon and ^{4}He

Calculated $^4He/^{40}Ar_{rad}$-production ratios based on U-, Th- and K-concentration measurements of 30 rock samples from reefs (conglomerates), hanging and footwall quartzites, volcanic rocks and dykes range from 7 to 184000 (Table 1). Very high U-concentrations were reported for the reefs, but not for the quartzite and volcanic rock samples originating from formations in the vicinity of the reefs (reviews by Koen, 1961; Pretorius, 1976, 1981; Hallbauer, 1986).

Observed $(^4He/^{40}Ar_{rad})_d$-ratios in the fissure water samples range from 1 to 27, with an average of 15.9 ± 6.7 (Table 3). This average value is significantly less than the $^4He/^{40}Ar_{rad}$ ratios calculated for the U-enriched reefs (Table 1) but within a factor of 3 above the average crustal rock production ratio (4.9). The $^4He/^{40}Ar_{rad}$ values also compare well with ^{4}He/

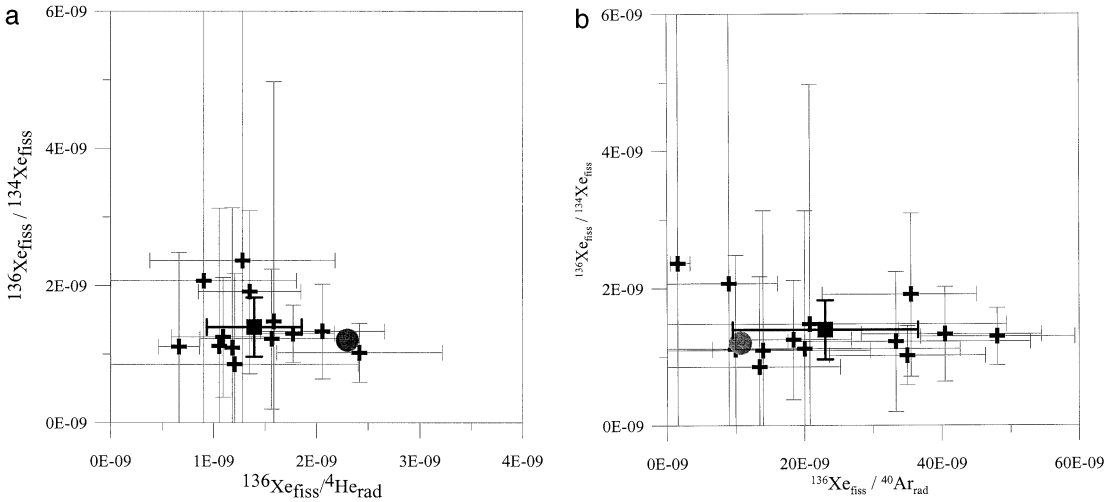

Fig. 7. **a:** $(^{136}Xe/^{134}Xe)_d$ versus $(^{136}Xe_{fiss}/^{4}He)_d$ of fissure water samples (cross symbols) compared to production ratios in the average crust (solid dot). The average $(^{136}Xe/^{134}Xe)_d$ (square) agrees with the production ratio, but the mean $^{136}Xe_{fiss}/^{4}He$ is too small by a factor of 2. This is explained by different release coefficients for He and Xe. **b:** $(^{136}Xe/^{134}Xe)_d$ versus $(^{136}Xe_{fiss}/^{40}Ar)_d$ of fissure water samples (cross symbols) compared to production ratios in the average crust (solid dot). The average $(^{136}Xe/^{134}Xe)_d$ ratios (square) agree with the crustal production ratio, but the average $^{136}Xe_{fiss}/^{40}Ar$-ratios are higher by a factor of 2.5. This can not be explained by the release coefficients, as $\lambda_{Ar} > \lambda_{Xe}$. This is explained by elevated U/K-ratios compared to the crustal average.

$^{40}Ar_{rad}$-ratios of hot springs in South Africa (Mazor and Verhagen, 1983) that range from 1 to 7.

Sample E5-46-Bh1 is exceptional with respect to the measured $^{4}He/^{40}Ar_{rad}$-ratio: The corrected ratio (Table 3) of 1.2 is the lowest in the data set and an order of magnitude smaller than the ratios of all other fissure water samples. Thus, like the [Cl], the $^{4}He/^{40}Ar_{rad}$-ratio also suggests that this fissure water is isolated from the fissure water network, where large-scale mixing/flow is likely to occur.

The observed ^{4}He-concentration of $0.3 \cdot 10^{-4}$cm^{3}STPg^{-1} in the dolomite aquifer (E4-IPC-DW-2) suggests a locally important crustal flux from the underlying sediments. The $^{4}He/^{40}Ar_{rad}$ ratio of the pore water (BE19BWBhDD13677; 26.3) is slightly higher than the average ratio of the fissure water and is similar to the local production ratio of the hanging wall quartzites (see Table 1, 'Beatrix, selected hanging and footwall'). However, the average $^{134}Xe_{fiss}/^{40}Ar_{rad}$ and $^{136}Xe_{fiss}/^{40}Ar_{rad}$ values of $(18.2 \pm 10.7) \cdot 10^{-9}$ and $(23.0 \pm 13.5) \cdot 10^{-9}$ are about a factor of two times higher than the calculated production ratios from average crustal U and K composition (2.8 ppm, 3.4%) of $8.9 \cdot 10^{-9}$ and $10.7 \cdot 10^{-9}$ (Fig. 7b).

Summarizing, the observed isotope ratios of individual elements ($^{3}He/^{4}He$, $^{40}Ar/^{36}Ar$ or $^{136}Xe_{fiss}/^{134}Xe_{fiss}$) each indicate a significant shift from air ratio and their signatures agree with radiogenic or fissiogenic production. Secondly, ratios of isotopes that originate from the same mother elements—$^{4}He/^{134}Xe_{fiss}$ and $^{4}He/^{136}Xe_{fiss}$—are enriched in respect to $^{-4}$He by a factor around 2. This is due to a larger release factor for He ($\lambda_{He} = 1$) than for Xe ($\lambda_{Xe} \sim 0.5$). Thirdly, ratios of isotopes that originate from different mother elements, ^{4}He and $^{134(136)}Xe_{fiss}$ on the one hand and $^{40}Ar_{rad}$ on the other, are likely affected by: *(a)* different release factors ($\lambda_{He} > \lambda_{Ar} > \lambda_{Xe}$) and *(b)* (U + Th)/K-concentration ratios in the host formations that are larger than crustal average composition.

4.4.8. Mixing and aging of fissure and pore water

With respect to the nucleogenic isotope concentrations, the process of ageing is indistinguishable from the process of mixing: Mixing of old water (with high nucleogenic noble gas isotope concentrations) with younger water would fall along a line with the same slope as the production line.

In Figure 8a raw data and corrected concentrations $(^{134}Xe_{fiss})_d$ are plotted versus $(^{4}He_{rad})_d$ concentrations. The corrected data fall within 2σ of the theoretical $^{134}Xe_{fiss}/^{4}He_{rad}$-production ratio of $1.9 \cdot 10^{-9}$ cm^3. The offset towards higher $^{4}He_{rad}$ concentrations can be explained by a greater release coefficient of He ($\lambda_{He} = 1$) than of Xe ($\lambda_{Xe} \sim 0.5$)

In Figure 8b raw data and $(^{134}Xe_{fiss})_d$ concentrations are plotted versus $(^{40}Ar_{rad})_d$. The theoretical $^{134}Xe_{fiss}/^{40}Ar_{rad}$-production line of $8.9 \cdot 10^{-9}$ for average crustal [U+Th]/K-ratio (Table 3) is indicated. The corrected fissure and pore water data fall (within 2σ) along this production line, but are systematically enriched in $^{134}Xe_{fiss}$. With $\lambda_{Ar} > \lambda_{Xe}$, the local formations must have a [U + Th]/K-ratio that is higher than the average crust. This is likely as some of the gold bearing formations in the area have remarkably high U concentrations (Table 1). This agrees with higher $(^{4}He_{rad}/^{40}Ar_{rad})_d$-ratios than expected in the average crust (Fig. 8c): Except for one sample (E5-46-Bh1) the $^{4}He_{rad}/^{40}Ar_{rad}$-ratios are 2–5 times larger than the $^{4}He_{rad}/^{40}Ar_{rad}$-production ratio in the average crust.

4.4.9. Calculation of the subsurface residence time

We calculate model ages in two scenarios with Eqn. 4.9 from the $(^{4}He_{rad})_d$, $(^{40}Ar_{rad})_d$, and $(^{134(136)}Xe_{fiss})_d$ concentrations. First, we consider only local production and no contribution from crustal fluxes and the expression for t_i in Eqn. 4.9 simplifies to $t_i = C_i/A_{is(i)}$. In a second scenario we additionally

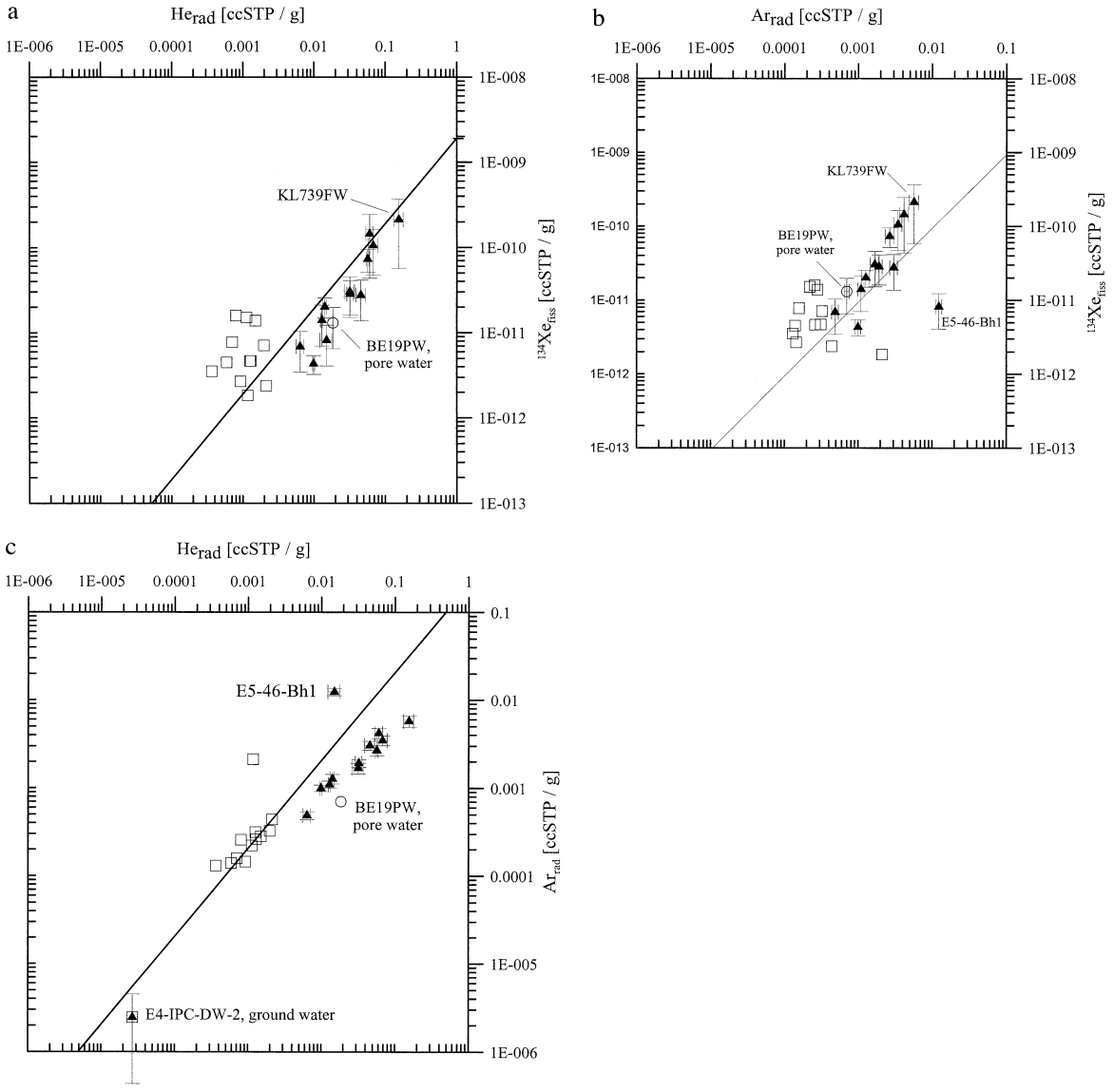

Fig. 8. a: Raw data (open rectangles) and corrected $^{134}Xe_{fiss}$ and $^{4}He_{rad}$ concentrations (solid triangles) of fissure and pore water samples (open circle). The corrected data fall along the theoretical $^{134}Xe/^{4}He$-production ratio of $1.9 \cdot 10^{-9}$ cm^3 from U (solid line). The small offset (within 2σ) towards higher $^{4}He_{rad}$ concentrations is due to a greater release coefficient ($\lambda_{He} > \lambda_{Xe}$) of He than for Xe. **b:** Raw data (open rectangles) and corrected concentrations (solid triangles) of $^{134}Xe_{fiss}$ versus $^{40}Ar_{rad}$ for the fissure and pore water samples; $^{134}Xe/^{40}Ar$ ratios are on average 2–3 times higher (see Table 3) than the average crustal production ratio. Therefore, the U/K-concentration ratio must be larger by a factor of 5 to 6 (2 times 2–3) than in the average crust to compensate for the release coefficient λ_{Xe} being smaller than λ_{Ar}. **c:** Raw data (open squares), corrected $^{40}Ar_{rad}$ versus $^{4}He_{rad}$ concentrations (solid triangles) and average crustal production (line). $^{4}He/^{40}Ar$ ratios are 2–5 the average crustal production ratio of $8.9 \cdot 10^{-9}$ (based on U = 2.8 ppm, Th = 10.8 ppm, and K = 3.4%). Assuming identical release coefficients for $\lambda_{He} = \lambda_{Ar} = 1$, this offset is interpreted to reflect an elevated [U + Th]/K-ratio compared to crustal average. The $^{40}Ar_{rad}$ concentration of E5-46-Bh1 is higher than expected according to average crustal production, and may be due to inherited $^{40}Ar_{rad}$ from metamorphic fluids; the $^{40}Ar_{rad}$ concentration of the ground water sample E4-IPC-DW2 is close to detection limit.

consider crustal flux contributions. (For both scenarios, assumptions include a porosity and density of $n = 0.01$ and $\rho_s = 2.6$ gcm^{-3}, $\lambda_{He} = \lambda_{Ar} = 1$ and crustal average K and Th concentrations of 3.4% and 10.4 ppm; Taylor and McLennan, 1995). The two parameters λ_{Xe} is varied between 0.1 and 1 and the U-concentration is varied between 1 and about 1000 ppm. For both scenarios, we fit the parameters λ_{Xe} and U for each sample individually to optimize the agreement between the calculated model ages t_{He}, t_{Ar} and t_{Xe} for each sample. In the second scenario we consider both, accumulation of in situ production (with only U as a variable parameter), and contributions from crustal flux components, J_{He}, J_{Ar}, and J_{Xe}. The gas flux from the aquifer to the atmosphere is assumed to be negligible. The geological structure of the Vredefort impact crater in the center of the Witwatersrand Basin offers the unique opportunity to sample rock material at shallow depth

Table 6. Calculated model ages according to two scenarios.

Sample	T_{xe_d} (A_{is134}) Ma	T_{xe_d} (A_{is138}) Ma	T_{he_d} (A_{is4}) Ma	T_{ar_d} (A_{is40}) Ma	λ_{xe}	[U] ppm	T_{he_d} (A_{is4} + A_j) Ma	T_{ar_d} (A_{is40} + A_j) Ma	T_{xe_d} (A_{is134} + A_j) Ma	T_{Xe} (A_{is136} + A_j) Ma	λ_{xe}	[U] ppm
BE19BWBhDD13677	16 ± 4	25 ± 1	21 ± 0	21 ± 2	0.30	26	0.9 ± 0.5	0.9 ± 0.5	0.6 ± 0.3	1.2 ± 0.6	0.33	520
BE16FW-GDW #1	51 ± 14	47 ± 2	51 ± 8	49 ± 7	0.31	18	2.0 ± 1.0	2.0 ± 1.0	1.9 ± 0.9	2.0 ± 1.0	0.32	400
BE16FW-GDW #3												
BE23FW-A4RD	35 ± 1	31 ± 1	33 ± 1	32 ± 3	0.38	10	1.1 ± 0.5	1.0 ± 0.5	1.1 ± 0.5	1.1 ± 0.6	0.38	230
BE24FW-C17W18 #2	45 ± 1	32 ± 1	37 ± 2	37 ± 5	0.42	10	1.2 ± 0.6	1.3 ± 0.7	1.4 ± 0.7	1.1 ± 0.6	0.44	230
BE325FW-CTS	92 ± 3	84 ± 2	90 ± 14	89 ± 10	0.20	14	4.8 ± 2.4	5.1 ± 2.5	4.8 ± 2.4	5.1 ± 2.5	0.20	220
BE327FW-CTS	52 ± 2	54 ± 2	54 ± 5	56 ± 6	0.30	17	3.6 ± 1.8	3.4 ± 1.7	3.2 ± 1.6	3.9 ± 1.9	0.32	210
B2-25-FW1 leak												
E4-IPC-DW-2												
E5-46-Bh1	(77) ± (3)	(151) ± (5)	(136) ± (26)	(364) ± (35)	1.00	1						
EV522FW-HWD	13 ± 0.44	16 ± 1	14 ± 2	14 ± 1	0.40	12	1.1 ± 0.6	1.2 ± 0.6	1.0 ± 0.5	1.4 ± 0.7	0.43	120
EV818FW-FBH	78 ± 5	79 ± 5	82 ± 4	79 ± 11	0.44	20	6.0 ± 3.0	6.0 ± 3.0	5.4 ± 2.7	6.4 ± 3.2	0.46	240
EV818FW-NEPD	129 ± 5	109 ± 5	119 ± 14	123 ± 16	0.75	14	9.5 ± 4.8	9.5 ± 4.7	9.6 ± 4.8	9.4 ± 4.7	0.80	140
K4-41-FW1b	21 ± 1	35 ± 1	28 ± 1	29 ± 2	0.22	9	3.9 ± 1.9	3.9 ± 1.9	2.7 ± 1.4	5.3 ± 2.7	0.23	45
K4-41-FW-2	95 ± 5	105 ± 5	98 ± 15	102 ± 13	0.52	20	13.2 ± 6.6	13.5 ± 6.8	12.0 ± 6.0	15.6 ± 7.8	0.55	130
KL739FW	158 ± 9	170 ± 8	165 ± 25	168 ± 25	0.45	28	20.2 ± 10.1	21.1 ± 10.6	18.0 ± 9.0	22.8 ± 11.4	0.48	210
W6-38-FW3 #1 leak												
W6-38-FW3 #1 leak												
W6-38-FW3 #2 leak												

Model ages calculated for fissure and pore water samples for two scenarios: The results in the left columns are based on accumulation of in situ production only (eq. 4.9 with $J_i = 0$ $cm^3STP\ cm^{-2}\ yr^{-1}$). The model ages listed on the right result from the scenario that considers crustal flues.

that is representative of the upper 14 km of the crust (Nicolaysen et al., 1981). The crustal composition below the Witwatersrand Triad indicates the production ratio P_4/P_{40} of 4.9 is an upper value for the Basin, as the U (and Th) concentration decreases with depth from about 3.6 ppm to 0.4 ppm (17.9 ppm to 6.6 ppm for Th) while the K concentrations remains constant around 3.4%. Thus, we may assume the He, Ar or Xe fluxes are identical or close to those derived from crustal average production. We use $J_{He} = 36 \cdot 10^{-7}$ $cm^3STPcm^{-2}yr^{-1}$ (Torgersen and Clarke, 1985) and $J_{Ar} = 7.3 \cdot 10^{-7}$ cm^3STP ^{40}Ar $cm^{-2}yr^{-1}$ with a ratio of $J_{He}/J_{Ar} = 4.9$ representing average crustal composition. J_{Xe} is estimated from:

$$J_{136_{Xe}} = \frac{P_{136}}{P_4} \cdot \frac{\lambda_{Xe}}{\lambda_{He}} \cdot J_{He} \; [cm^3STP^{136}Xe\ cm^{-2}yr^{-1}] \tag{4.17}$$

with a production ratio for $^{136}Xe/^4He$ of $P_{136}/P_4 = 2.3 \cdot 10^{-9}$, and a release factor of $\lambda_{He} = 1$. With an assumed release coefficient of $\lambda_{Xe} = 0.5$ the estimated crustal Xe-flux according to Eqn. 4.17 would amount to ~35 ^{136}Xe atoms $m^{-2}s^{-1}$. This agrees with results from Drescher et al. (1998) who stated an upper limit of the continental crustal degassing flux of 60 ^{136}Xe atoms $m^{-2}s^{-1}$. For *h*, the thickness of the structure within which the crustal fluxes accumulate (see Eqn. 4.9), we use the individual sample depth of the fissure waters (Table A1). If it is assumed that nucleogenic isotope concentrations always increase with depth, then applying the observed concentration at the maximum depth of the layer of thickness *h* is equivalent to assuming the measured concentration to be the maximum concentration in that layer. If the nucleogenic isotope concentration profiles are linear, the calculation can only be high by a factor of two since the nucleogenic isotope concentration at depth = zero is approximately zero. Furthermore, as we do not know either there was any loss of gas into the atmosphere, the minimum age is calculated. The resulting model ages calculated for in situ only are listed in the left-hand block in Table 6; the results of in situ plus crustal flux are listed in the right-hand block. For both scenarios, the individual model ages t_i (with i = He, Ar and Xe) can be brought to agreement for all samples (except E5-46-Bh1) by fitting the two parameters λ_{Xe} and U. Second, release coefficients in both scenarios, $0.20 < \lambda_{Xe} < 0.80$, are rather high compared to Ragettli et al. (1994) and therefore, the t_{Xe} model ages may underestimate the subsurface residence time. Third, the U-concentration in the local formations (9–28 ppm for in situ only; 45–520 ppm for in situ plus crustal flux) represent the average U-concentration in those formations that are intersected by the network of fissures from which the water samples are derived. Both sets of U-concentrations are not unlikely. In the first scenario, the U-concentrations are 3 to 10 times higher than crustal average, but such values have been analysed in the hanging and footwall formations in the vicinity of the sampling sites (Table 1). In the second scenario, this influence of the local formation on the fissure water concentrations is overprinted by the contribution of the crustal flux components. Here the U-concentrations in the local formations are close to those observed in some selected reefs (Table 1). For the pore water sample, this second scenario seems to produce unrealistically high average U-concentration (520 ppm); the average concentration of 10 quartzite samples from the hanging and footwall at Beatrix mine is (74 ± 75) ppm.

The model ages derived without a crustal flux contribution range between 13 and 168 Ma for the individual samples, the model ages derived with a crustal flux contribution range between 1 and 23 Ma. Within the uncertainty of these model ages, both model ages indicate all samples are older than 1.5 Ma. We consider the results of the first scenario to be maximum ages and the second scenario to be minimum ages. Given the high [U] necessary to fit the noble gas measurements and the measured [U] in local rock the first scenario results might represent better estimates of the subsurface residence time.

In section 4.2 the ^{36}Cl-data could not unambiguously be interpreted. There was still the possibility of interpreting the water as significantly younger than 1.5 Ma by leaching Cl with a $^{36}Cl/Cl$-ratio in secular equilibrium concentration from the formations. With a comparison to the noble gas model ages, it seems likely that all the fissure water samples are older than 1.5 Ma. Fissure water $^{36}Cl/Cl$-ratios ($4 \cdot 10^{-15}$ to $37 \cdot 10^{-15}$) can reflect secular equilibrium in formations with U-concentrations of 9 to 29 ppm (first scenario), but would be too low in formations with 45 to 520 ppm U (second scenario).

The influence of the assumed Xe crustal flux on the overall model ages in the second scenario is very small and could fully be explained by slightly increasing the release coefficient λ_{Xe}. This data set is thus not suitable to determining whether a crustal Xe-flux exists or not.

4.4.10. Sample E5-46-Bh1

The fractionation pattern of sample E5-46Bh1 is best explained as degassing at 70–120°C, significantly above the sampling temperature of 37.2°C. For any other fissure water sample, this finding could lead to the conclusion that the water is upwelling from even greater depths. A temperature of 90°C would correspond to an unrealistic great depth of about 10 km, using the observed local geothermal gradient of only 9°/km (Nicolaysen et al., 1981; Omar et al., 2003). But E5-46-Bh1 shows distinct evidence of originating from an isolated, highly saline water pocket that has been draining since it was intersected in 1996. Thus, we suggest that this temperature reflects the formation temperature of the site, similar to the closure temperature of a fluid inclusion than the formation temperature at greater depth.

Following this interpretation, the $\delta^{18}O$ value of E5-46-Bh1, indicates that it has been significantly affected by water-rock interactions. The $\delta^{18}O$ represents either in situ weathering of silicates or low temperature precipitation of clay. During either of these alteration processes radiogenic ^{40}Ar would be released from the rock matrix into the pore fluids. Alternatively, this fissure water may represent a metamorphic fluid that formed at 350°C 2.05Ga ago and was affected by degassing of local rock as the formation cooled to 70–120°C. According to Omar et al. (2003), this formation temperature (70–120°C) was reached about 80 Ma before today. If this is true, then these metamorphic fluids should have been sterile until they were intersected by the mining activities. In any case, assuming this water pocket to be isolated and sealed for geologic times scales, the accumulation of crustal flux during its subsurface residence time would—like fluid inclusions—contribute only minor

amounts to the total observed $^{40}Ar_{rad}$ concentration. Thus, the total observed nucleogenic gases rather reflect the nucleogenic concentrations of the metamorphic fluids, that is gradually increasing since the inclusion formed and is due only to in situ production.

In Table 6, model ages for E5-46-Bh1 are calculated only for the scenario without crustal flux contribution and we consider U-concentrations as in the average crust (2.8 ppm) since any influence of elevated U-concentrations from a U-bearing reef located in some distance is excluded. On average, the model ages of $^{134(136)}Xe_{fiss}$ (77 ± 3) Ma (151 ± 5 Ma) and $^{4}He_{rad}$ (136 ± 26) Ma deviate from the Ar_{rad} model age of (364 ± 35) Ma by a factor of larger 3. This discrepancy indicates that the "dating"-method applicable on all other fissure water samples should not be applied here. These calculated model ages are the least reliable in the data set. First, in such a water pocket the 'porosity' significantly exceeds the value of n = 0.01 that is assumed in the model. Secondly, the quantity of inherited nucleogenic gas concentration of this particular sample is unknown. And third, the model result of the degassing temperature of 70°C supports the interpretation of a metamorphic fluid and Eqn. 4.9 and the following are not applicable.

5. IMPLICATIONS WITH RESPECT TO THE DEEP BIOSPHERE

It is known from apatite dating (Omar et al., 2003), that the Ventersdorp Supergroup located at Driefontein Gold Mines at a depth of 3.7 km bs (below surface) did not cool below 120°C until 90 million years ago. The corresponding maximum temperatures at the depths where the fissure water samples were collected (3.1 km bs) would have been ca. 110–115°C, which is at the upper temperature limit for the hyperthermophilic microbes. Fissure waters that yield t_{Xe} model ages exceeding 90 Ma must therefore be sterile or we must assume some mixing has occurred. Non-sterile fissure water (containing apparently indigenous thermophilic microorganisms) indicates mixing between fissure water from greater depth with even greater nucleogenic isotope concentrations, and hence more ancient age, and microorganism-bearing ground water from more moderate depths.

Microbes inhabiting ground water with temperatures below about 120 °C are well-adapted (thermophilic or hypertermophilic) to colonize the deeper, sterilized subsurface as the formation cools at 1°C/Ma or equivalent to migrating downwards at a rate of 50–100 m/Ma.

In the case of E5-46-Bh1, no hyperthermophilic DNA signatures were recovered, but some deeply rooted bacterial 16SrDNA sequences were found that may represent ancient inhabitants of this fissure (Moser et al., 2003) and further examination of their physiology is being pursued.

In the case of less saline water, e.g., K4-41-FW1b, 16SrDNA that is 99% similar to the hyperthermophile, Pyrococcus Abysii was recovered. The t_{Xe} model ages for this fissure water range from (11 ± 6) Ma to (17 ± 9) Ma. From this we infer that this environment has been open to groundwater circulation and hence microbial migration and colonization since 90 Ma and that the Pyrococcus Abysii represents a subsurface inhabitant from greater than 3.3 km bs that has been carried upwards with the older groundwater enriched in nucleogenic isotopes.

The similarity in the calculated residence times for the pore water and the fissure water samples suggests isotopic equilibrium between the pore water and fracture associated fissure water exists. This can be attained only when the fluid flow is extremely slow and extends over long and deep subsurface pathways; otherwise the fissure water would be expected to be much younger. This slow movement of fissure water does not contradict the interpretation of mixing along extended horizontal and vertical pathways. Omar et al. (2003) estimated vertical fluid velocities of <3 km Ma up to -1 based upon a 1-D fluid advection model and measured geothermal gradients. This fluid velocity and the above residence times suggest that the subsurface flow path distances vary from 1 to 300 km.

6. CONCLUSIONS

1. Thirteen fissure water samples, one pore water and one ground water sample were collected from localities widely dispersed over the Witwatersrand Basin covering a depth range up to 3.3 km.
2. All fissure water samples are significantly (70–98%) undersaturated with respect to the Ne concentration of ASW at 20°C and 1013 mbar. The elemental fractionation pattern of the atmospheric noble gases identifies two processes that cause this undersaturation both originating as a result of depressurization of the formation with the mining activities.
3. A simple model reproduces the fractionation pattern of all individual samples and allows the correction of the observed gas losses.
4. Ten of the fissure water samples reflect an elemental fractionation pattern that can be explained by diffusive degassing at the sampling temperature (BE16FW-GDW #1, BE23FW-A4RD, BE24FW-C17W18 #2, BE325FW-CTS, BE327FW-CTS, EV522FW-HWD, EV818FW-FBH, EV818FW-NEPD, K4-41-FW-2, KL739FW).
5. Two fissure water samples reflect a fractionation pattern that is best reproduced by combined processes of diffusive degassing and solubility equilibrium with an open gas phase at sampling temperature (BE16FW-GDW#3, K1-41-FW1b). We suggest that this gas phase developed recently during mining activity.
6. For one water sample (E5-46-Bh1), the applied conceptual model can best explain the results when we assume the diffusive degassing has occurred at temperatures significantly above sampling temperature (70 to 120°C).
7. These results indicate that two different types of deep subsurface water were encountered in the Witwatersrand Basin:
   - The majority of water samples are moderately saline fissure waters that originate from a network of water-bearing fractures that channel fluid flow. The basin-wide existence of these potential pathways for vertical and horizontal fluid flow is well documented. This type of fissure water is interpreted to originate from an extended network of water-bearing fractures, always associated with faults and dykes; with long residence times in the subsurface and migrating along extended pathways.
   - The second fissure water type is distinctively more saline and is significantly affected by water-rock interaction. It is interpreted to originate from hydrologically isolated water pockets. This water type is characterized by sample E5-

46-Bh1 that likely originates from an isolated water pocket of metamorphic fluids similar to a huge fluid inclusion. The calculated degassing temperature of 70–120°C is interpreted to reflect the temperature of the sampling site back in time, similar to the closure temperature of a fluid inclusion.

8. The combined interpretation of the noble gas model ages and the ^{36}Cl-content of the fissure water samples indicates subsurface water (and therefore microbe) residence times older than 1.5 Ma. The measured ^{36}Cl concentrations are identical to calculated secular equilibrium concentrations based on the radioelement concentrations as reported for the Klipriviersberg Lava.
9. From the nucleogenic noble gas isotope concentrations, $\lambda_{He} = \lambda_{Ar} = 1$, K = 3.4% and Th = 10.8 ppm, model ages for two scenarios (with and without a contribution of crustal flux components) are calculated (with λ_{Xe} and the U-concentration in the local formation as free parameters to optimize the agreement of the model ages t^{134}_{Xe}, t^{136}_{Xe}, t^{40}_{Ar}, and t^{4}_{He}.), With only local production, the model ages for individual samples are 13–168 Ma (except E5-46-Bh1, that is considered to be a metamorphic fluid). When a crustal flux is considered model ages for individual samples are 1–23 Ma and are considered minimum subsurface residence times. ^{36}Cl/Cl-ratios might favor the first scenario as the more likely

Acknowledgments—We thank the subsurface sampling team members Julie Ward and Dr. Greg Slater for their excellent cooperation. We are grateful to Bob Wilson of Turgis-SRK Technologies for advising us on numerous questions during the course of the field project. We also thank Andy Makkink (geologist) and Jan Meinties (drilling manager) at Beatrix Mine 1 shaft enabling us to sample a freshly drilled core. We gratefully acknowledge Paul Penner (mine manager), Colin Rolston, Walter Seymoor and Danie Thompson (geologists) at Evander Mine for their support during sampling. We also wish to thank Dr. Davie Nel of East Driefontein Mine for providing us the stratigraphy of the mine. Dr. Esta van Heerden and Prof. Dereck Litthauer from Free State University kindly provided lab space and logistical support to our project. Special thanks to Prof. Peter Schlosser, LDEO; furthermore to Ralph Gardner and Paul Betts, NEVIS Labs, Columbia University for the design and manufacturing of the pore water sampling containers. We also thank Prof. David Elmore and Dr. Mike Bourgeois from Purdue University for providing us with details regarding the AgCl precipitation, and Prof. Balt Verhagen at the Schonland Research Centre, Witwatersrand University as co-operating laboratory of the GNIP database.

This manuscript benefited from valuable comments and constructive criticism by Prof. Chris Ballentine and two anonymous reviewers.

This work was supported by the German Science Foundation DFG (Deutsche Forschungsgemeinschaft) Li-872/1-1 and grant EAR-9714214 from the National Science Foundation LExEn program to Princeton University (T.C. Onstott). This is LDEO contribution #6467.

Associate editor: D. Cole

REFERENCES

Aeschach-Hertig W., Peeters F., Beyerle U., and Kipfer R. (1999) Interpretation of dissolved atmospheric noble gases in natural waters. *Wat. Res. Res.* **35,** 2779–2792.

Andrews J. N. (1985) The isotopic composition of radiogenic Helium and its use to study groundwater movement in confined aquifers. *Chem. Geol.* **49,** 339–351.

Andrews J. N. and Lee D. J. (1979) Inert gases in groundwater from the Bunter Sandstone of England as indicators of age and paleoclimatic trends. *J. Hydrol.* **41,** 233–252.

Andrews J. N. and Wilson G. B. (1987) The composition of dissolved gases in deep groundwater and groundwater degassing. In *Saline Waters and Gases in crystalline rocks, Geolog. Ass. of Can.* (eds. P. Fritz and S. K. Frape) Special Paper, **33,** 245–252.

Andrews J. N., Davis S. N., Fabryka-Martin J., Fontes J. Ch., Lehmann B. E., Loosli H. H., Michelot J. L., Moser H., Smith B., and Wolf M. (1989) The in-situ production of radioisotopes in rock matrices with particular reference to the Stripa granite. *Geochim. Cosmochim. Acta* **53,** 1803–1815.

Antrobus E. S. A., Brink W. C. J., Caulkin J., Hutchinson R. I., Thomas D. E., Van Graan J. A., and Viljoen J. J. (1986) The Klerksdorp Goldfield. (eds. C. R. Anhaeusser and S. Maske) *Geol. Soc. S. Afr., Min. Dep. of S. Afr.* **1,** 549–598.

Armstrong R. A., Compston W., Retief E. A., Williams I. S., and Welke H. J. (1991) Zircon ion-microbe studies bearing on the age and evolution of the Witwatersrand Triad. *Precamb. Res.* **53,** 243–266.

Ballentine C. J., O'Nions R. K., Oxburg E. R., Horvath F., and Deak J. (1991) Rare gas constraints on hydrocarbon accumulation, crustal degassing and groundwater flow in the Permian Basin. *Earth Planet. Sci. Lett.* **103,** 229–246.

Ballentine C. J., Mazurek M., and Gautschi A. (1994) Thermal constraints on crustal rare gas release and migration: Evidence from Alpine fluid inclusions. *Geochim. Cosmochim. Acta* **58,** 4333–4338.

Ballentine C. J., O'Nions R. K., and Coleman M. L. (1996) A Magnus opus: helium, neon, and argon isotopes in a North Sea oilfield. *Geochim. Cosmochim. Acta* **60**(5), 831–849.

Bentley H. W., Phillips F. M., and Davis S. N. (1986) Handbook of Environmental Isotope Geochemistry, Vol. **2**, the Terrestrial Environment, B. (eds. P. Fritz and J. Ch. Fontes), Elsevier, New York, 1986, 427.

Boston P. J., Ivanov M. V., and McKay C. P. (1992) On the possibility of chemosynthetic ecosystems in subsurface habitats on Mars. *Icarus* **95,** 300–308.

Bosch A. and Mazor E. (1988) Natural gas association with water and oil as depicted by atmospheric noble gases: case study from the southeastern Mediterranean Coastal Plain. *Earth Planet. Sci. Let.* **87,** 338–346.

Brand E. L. (1986) Water and gas occurrences in the Evander Goldfield. (eds. C. R. Anhaeusser and S. Maske). *Geol. Soc. S. Afr., Min. Dep. of S. Afr.* **1,** 797–809.

Cano R. J. and Borucki M. (1995) Revival and identification of bacterial spores in 25 to 40 million year old Dominican amber. *Science* **268,** 1060–1064.

Castro M. C., Stute M., and Schlosser P. (2000) Comparison of ^{4}He ages and ^{14}C ages in simple aquifer systems: implications for groundwater flow and chronologies. *Appl.Geochem.* **15,** 1137–1167.

Craig H. (1961) Isotopic variations in meteoric waters. *Science* **133,** 1702–1703.

Crovetto R., Fernandez-Prini R., and Jaspas M. L. (1982) Solubilities of inert gases and methane in H_2O and in D_2O in the temperature range of 300 to 600 K. *J. Chem. Phys.* **76**(2), 1077–1086.

de Wit M. J., Roering R., Hart R. J., Armstrong R. A., De Ronde C. E. J., Green R. E. W., Tredoux M., Peberdy E., and Hart R. A. (1992) Formation of an Archaean continent. *Nature* **357,** 553–562.

Duane M. J., Pigozzi G., and Harris C. (1997) Geochemistry of some deep gold mine waters from the western portion of the Witwatersrand Basin, South Africa. *J. Afr. Earth Sic.* **24**(1/2), 105–123.

Drescher J., Kirsten T., and Schaefer K. (1998) The rare gas inventory of the continental crust, recovered by the KTB Continental Deep Drilling Project. *Earth Planet. Sci. Lett.* **154,** 247–263.

Driefontein Consolidated Limited (1998) Transverse section through No 7-W, No 1-E and No5-E shafts looking East (30-06-1998) *unpublished*.

Elliot T., Ballentine R. K., O'Nions R. K., and Ricchiuto T. (1993) Carbon, helium, neon and argon isotopes in a Po Basi n (northern Italy) natural gas field. *Chem. Geol.* **106,** 429–440.

Elmore D., Fulton B. R., Glover M. R., Mardsen J. R., Gove H. E., Naylor H., Purser K. H., Kulius L. R., Beukens R. P., and Litherland

A. E. (1979) Analysis of ^{36}Cl in environmental water samples using an electrostatic accelerator. *Nature* **277,** 22–25.

Eyring H. (1936) Plasticity and diffusion as examples of absolute reaction rates. *J. Chem. Phys.* **4,** 283–291.

Fabryka-Martin J. T., Davis R., and Elmore D. (1987) Applications of ^{129}I and ^{36}Cl in hydrology. *Nucl. Instr. Meth. Phys. Res.* **B29,** 361–371.

Fontes Ch. J. (1989) The Chlorine-36 method. In *Nuclear Methods of Dating* (eds. E. Roth and B. Poty), Chap. 14, pp. 397–398. CEA, Paris Printed in the Netherlands.

Grieve R. A. F., Coderre J. M., Robertson P. B., and Alexopoulos J. (1990) Microscopic planar deformation features in quartz of the Vredefort structure: Anomalous but still suggestive of an impact origin. *Tectonophys.* **171,** 185–200.

Hallbauer D. K. (1986) The Mineralogy and Geochemistry of Witwatersrand Pyrite, Gold and Uranium, and carbonaceous matter. (eds. Anhaeusser C.R., and Maske, S.). *Geol. Soc. S. Afr., Min. Dep. of S. Afr.* **1,** 731–752.

Hamano Y. and Ozima M. (1978) Earth-atmosphere evolution model based on Ar isotopic data. In *Terrestrial Rare Gases,* **3** (eds. E. C. Alexander and M. Ozima)155–172. Jpn. Sci. Soc. Press, Tokyo Adv. Earth Planet. Sci., 1079.

Handley J. R. F (1990) World gold resources review at the end of the 1980 decade. *Univ. Witwatersrand Econ. Geol. Res. Unit. Inf. Circ.* **227,** 37. pp.

Heaton T. H. E. (1981) Dissolved noble gases: some applications to groundwater research. *Trans. Geol. Soc. S. Afr.* **84,** 91–97.

IAEA/WMO (2002) Global Network for Isotopes in Precipitation. The GNIP Database. Accessible at: http://www.iaea.org/programs/ri/gnip/gnipmain.htm.

Jähne B., Heinz G., and Dietrich W. (1987) Measurement of the diffusion coefficients of sparingly soluble gases in water. *J. Geophys. Res.* **92,** C10., 10767–10776.

Karl D. M. (1995) The microbiology of deep-sea hydrothermal vents. CRC Press Boca Raton, 299 pp.

Karl D. M., Bird D. F., Björkman K., Houlihan T., Shackelford R., and Tupas L. (1999) Microorganisms in the accreted ice of Lake Vostok, Antarctica. *Science* **268,** 2144–2147.

Kieft T. L., Fredrickson J. K., Onstott T. C., Gorby Y. A., Kostandarithes H. M., Bailey T. J., Kennedy D. W., Li S. W., Plymale A., Spadoni C. M., and Gray M. S. (1999) Dissimilatory reduction of Fe(III) and other electron acceptors by a Thermus isolate. *Appl. Environ. Microbiol.* **65,** 1214–1221.

Klemd R., Hallbauer D. K., and Barton J. M. (1989) Fluid inclusions studies of hydrothermally altered archaean granites around the Witwatersrand Basin. *Min. Petrol.* **40,** 39–56.

Koen G. M. (1961) The genetic significance of the size distribution of Uranitite in Witwatersrand Bankets. *Trans. Proc. Geol. Soc. S. Afr.* **64,** 23–54.

Lal D. and Peters B. (1967) Cosmic ray produced radioactivity on the Earth. In *Handbuch der Physik,* (ed. K. Sitte) **42/2**, pp. 551–612. Springer Verlag, Berlin.

Leroux H., Reimold W. U., and Doukhan J. C. (1994) A TEM investigation of shock metamorphism in quartz from the Vredefort Dome, South Africa. *Tectonophys.* **230,** 223–239.

Lippmann J (1998) Determination of pore water dynamics in low permeable geological formations around ERA Morsleben by isotope and noble gas measurements. Ph. D. thesis, Heidelberg University, Germany.

Lippold H. J. and Weigel E. (1988) ^{4}He diffusion in ^{40}Ar-retentive minerals. *Geochim. Cosmochim. Acta* **52,** 1449–1458.

Martel D. J., O'Nions R. K., Hilton D. R., and Oxburgh E. R. (1990) The role of element distribution in production and release of radiogenic helium: The Carnmenellis granite southwest England. *Chem. Geol.* **88,** 207–221.

Marty B. (1984) On the noble gas isotopic fractionation in naturally occurring gases. *Geochim. J.* **18,** 157–162.

Mazor E. (1972) Paleotemperatures and other hydrological parameters deduced from noble gases dissolved in groundwaters, Jordan Rift Valley. *Geochim. Cosmochim. Acta* **36,** 1321–1336.

Mazor E. and Verhagen, B. T. (1983) Dissolved solids, stable isotopes and radioactive isotopes and noble gases in thermal waters of South Africa. *J. Hydrol.* **63,** 315–329.

Moser D. P., Takai K., Balkwill D. L., Fredrickson J. K. and Onstott T. C. (2001) Molecular characterizations of microbial diversity in fissure waters and Carbon Leader Ore from Ultra-deep South African Au mines. *Abstr. ASM Ann. Mtg.* Orlando, Fl., May. 2001.

Moser D. P., Onstott T. C., Balkwill D., Takai K., Pfiffner S., White D. C., Baker B., Brockman F. J., Fredrickson J. K., Sherwood Lollar B., Slater G., Pratt L. M., Fong J., Phelps T. J., Spoelstra N. and DeFlaun M. (2002) Microbial community and water Chemistry Changes in a Borehole from an Ultradeep South African Gold Mine. submitted.

Moser D. P., Martin H. W., and Boston P. J. (2003) Caves and Mines Microbiological Sampling. In *Encyclopedia of Environmental Microbiology.* John Wiley and Sons, Inc. DOI:10.1002/0471263397.env276.

Nicolaysen L. O., Hart R. J., and Gale N. H. (1981) The Vredefort radioelement profile extended to supracrustal strata at Carletonville, with implications for continental heat flow. *J. Geophys. Res.* **86(**B11**),** 10653–10661.

Omar G., Onstott T. C., and Hoek J. (2003) The origin of deep subsurface microbial communities in the Witwatersrand Basin, South Africa ad deduced from apatite fission track analyses. *Geofluids* **3,** 69–80.

Onstott T. C., Moser D. P., DeFlaun M. F., Pratt L. M., Pfiffner S. and Sherwood-Lollar B. (2001) Geohydrological and biogeochemical subsurface environments within the Witwatersrand Basin, South Africa. *Abstr. ASM Ann. Mtg.* Orlando, Fl., May. 2001.

Osenbrück K., Lippmann J., Sonntag Ch. (1998) Dating very old pore waters in impermeable rocks by noble gas isotopes *Geochim. Cosmochim. Acta* **62,** 3041–3045.

Ozima M. and Podosek F. A. (1983) Noble Gas Geochemistry. Cambridge Univ. Press.

Pedersen K. (1997) Microbial life in deep granitic rock. *FEMS Microbiol. Rev.* **20**(2–3), 399–414.

Pinti D. L. and Marty E. (1995) Noble gases in crude oils from the Paris Basin, France: Implications for the origin of fluids and constraints on oil-water interactions. *Geochim. Cosmochim. Acta* **59,** 3389–3404.

Pinti D. L. and Marty B. (1997) Evaluating fluid circulation in deep sedimentary aquifers: the noble gas approach from the Paris Basin. In *GEOFLUIDS '97, an International Conference on Fluid Evolution, Migration and Interaction* (eds. J. P. Hendry et al.) 46–49.

Pretorius D. A. (1976) The nature of the Witwatersrand gold-uranium deposits. In *Handbook of Stratabound and Stratiform Ore Deposits* (ed. K. H. Wolf) 29–88. Elsevier.

Pretorius D. A. (1981) Gold and Uranium in quartz-pebble conglomerates. *Econ. Geol.* **75,** 117–138.

Priscu J. C., Adams E. E., Lyons W. B., Voytek M. A., Mogk D. W., Brown R. L., McKay C. P., Takacs D. D., Welch K. A., Wolf C. F., Krishtein J. C., and Avci R. (2001) Geomicrobiology of subglacial ice above Lake Vostok, Antarctica. *Science* **288**(5447), 2141–2144.

Ragettli R. A., Hebeda E. H., Signer P., and Wieler R. (1994) Uranium-Xenon chronology: precise determination of $\lambda_{sf} \cdot {}^{136}Y_{sf}$ for spontaneous fission of ^{238}U. *Earth Planet Sci. Lett.* **128,** 653–670.

Reimold W. U., Meshik A. P., Smits G., Pravdivtseva O. V., and Shukolyukow Y. A. (1995) Fission xenon dating of Witwatersrand uraninites: Implications for geological acrivity in the Central Kaapvaal Craton about 1 Ga ago. *Geochim. Cosmochim. Acta* **59**(24), 5177–5.

Robb L. J. and Meyer F. M. (1995) The Witwatersrand Basin, South Africa: Geological framework and mineralization processes. *Ore Geol. Rev.* **10,** 67–94.

Robb L. J., Charlesworth, E. G., Drennan G. R., Gibson R. L., and Tongu E. L. (1997) Tectono-metamorphic setting and paragenetic sequences of Au-U mineralisation in the Archaean Witwatersrand Basin, South Africa. *Austr. J Earth Sci.* **44,** 353–371.

Rudolph J., Rath H. K., and Sonntag Ch. (1983) Noble gases and stable isotopes in ^{14}C-dated paleowaters from Central Europe and the Sahara IAEA-SM-270/17, 1983.

Rübel A. P., Sonntag Ch., Lippmann J., Pearson F. J., and Gautschi A. (2002) Solute. Transport of formations of very low permeability: Profiles of stable isotopes and noble gas contents in the Opalinus Clay, Mont Terri, Switzerland. *Geochim. Cosmochim. Acta* **66(8),** 1311–1321.

Shukoljukov J., Kirsten T., and Jessberger E. K. (1974) The Xe-Xe spectrum technique, a new dating method. *Earth Planet. Sci. Lett.* **24,** 271–291.

Solomon D. K., Hunt A., and Poreda R. J. (1996) source of radiogenic ^{4}He in shallow aquifers; implications for young groundwater. *Wat. Res. Res.* **32**(6), 1805–1813.

Stute M (1989) Edelgase im Grundwasser: Bestimmung von Paläotemperaturen und Untersuchung der Dynamik von Grundwasserfliebsystemen. *Ph. D. thesis*, University of Heidelberg, Germany.

Stute M., Clark J. F., Schlosser P., Broecker W. S., and Bonani G. (1995a) A 30,000 yr continental paleotemperature record derived from noble gases dissolved in groundwater from the San Juan Basin, New Mexico. *Q. Res.* **43,** 209–200.

Stute M., Forster M., Frischkorn H., Sarejo A., Clark J. F., Schlosser P., Broecker W. S., and Bonani G. (1995b) Cooling of the tropical Brazil (5°C) during the last glacial maximum. *Science* **269,** 379–383.

Stute M., Sonntag Ch., Deak J., Schlosser P. (1992a) Helium in deep circulating groundwater in the Great Hungarian Plain: Flow dynamics and crustal and mantle helium fluxes. *Geochim. Cosmochim. Acta* **56,** 2051–2067.

Stute M., Schlosser P., Clark J. F., and Broecker W. S. (1992b) Paleotemperatures in the southwestern United States derived from noble gases in groundwater. *Science* **246,** 1000–1003.

Takai K., Moser D. P., DeFlaun M., Onstott T. C., and Fredrickson J. K. (2001) Archael diversity in waters from deep South African gold mines. *Appl. Envir. Micobiol.* **67**(12), 5750–5760.

Takai K., Moser D. P., Onstott T. C., Spoelstra N., Pfiffner S. M., Dohnalkova A. and Fredrickson J. K. (2001) Alcaliphilus transvaalensis gen. nov., sp. nov., an extremely alkaliphilic bacterium isolated from a deep South African gold mine. *Int. J. Syst. Evol. Microbiol.* **51,** 1245–1256.

Taylor S. R. and McLennan S. M. (1985) The Continental Crust: Its Composition and Evolution. Blackwell Sci. Publ., Boston, Mass., 312pp.

Tolstikhin I., Lehmann B. E., Loosli H. H., and Gautschi A. (1996) Helium and Argon isotopes in rocks, minerals, and related groundwaters: A case study in northern Switzerland. *Geochim. Cosmochim. Acta* **60**(9), 1497–1514.

Torgersen T. (1980) Controls on pore-fluid concentration of ^{4}He and ^{222}Rn and the calculation of ^{4}He/^{222}Rn ages. *J. Geochem. Explor.* **13**(1), 57–75.

Torgersen T. and Clarke W. B. (1985) Helium accumulation in groundwater, I: An evaluation of sources and the continental flux of crustal ^{4}He in the Great Artesian Basin, Australia. *Geochim. Cosmochim. Acta* **49,** 1211–1218.

Torgersen T. and Ivey G. N. (1985) Helium accumulation in groundwater, II: a model for the accumulation of the crustal ^{4}He degassing flux. *Geochim. Cosmochim. Acta* **49,** 2445–2452.

Torgersen T., Kennedy B. M., Hiyagon H., Chiou K. Y., Reynolds J. H., and Clarke W. B. (1989) Argon accumulation and the crustal degassing flux of ^{40}Ar in the Great Artesian Basin, Australia. *Earth Planet. Sci. Lett.* **92,** 43–56.

Torgersen T., Habermehl M. A., Phillips F. M., Elmore D., Kubik P., Jones B. G., Hemmick T., and Gove H. E. (1991) Chlorine 36 Dating of Very Old Groundwater. 3. Further Studies in the Great Artesian Basin, Australia. *Wat. Res. Res.* **27**(no.12), 3201–3213.

Torgersen T. and O'Donnell J. (1991) The degassing flux from the solid earth: Release by fracturing. *Geophys. Res. Lett.* **18**(5), 951–954.

Torgersen T. and Kennedy B. M. (1999) Air-Xe enrichments in Elk Hills oil field gases: role of water in migration and storage. *Earth Planet. Sci. Lett.* **167,** 239–253.

Tweedie E. B. (1986) The Evander Goldfield. Mineral Deposits of Southern Africa. (eds. C. R. Anhaeusser and S. Maske) **1 & 2,** *Geol. Soc. S. Afr., Min. Dep. of S. Afr.* 705–730.

Tweedie K. A. M. (1986) The discovery and exploitation of Beisa and Beatrix Gold and Uranium Mines in the southern extension of the Welkom Goldfield. (eds. C. R. Anhaeusser and S. Maske) **1 & 2,** *Geol. Soc. S. Afr., Min. Dep. of S. Afr.* 541–547.

Vegter J. R. and Foster B. J. (1992) the Hydrology of dolomitic formations in the southern and westen Transvaal. *Int. Contrib. To Hydrogeol.* **13,** 355–376.

Vreeland R. H., Rosenzweig W. D., and Powers D. W. (2000) Isolation of a 250 million-year-old halotolerant bacterium from primary salt crystal. *Nature* **407,** 897–900.

Wasserburg G. J., Mazor E., and Zartman R. E. (1963) Isotopic and chemical composition of some terrestrial natural gases. In *Earth Science and Meteorites* (eds. J. Geiss and E. P. Goldberg) pp 219–240. North Holland, Amsterdam, 1963.

Wasserburg G. J. and Mazor E. (1965) Spontaneous fission xenon in natural gases. In *Fluids in subsurface environments*, Symposium AAPG, 1965; 386–398.

Whiteside H. C. M, Glasspool K. R., Hiemstra S. A. (1986) Gold in the Witwatersrand Triad. *Min. Res. Rep. S. Afr.* (ed. C. B. Coetze), 5th ed., 39–73.

Zartman R. E., Wasserburg G. J., and Reynolds J. H. (1961) Helium, argon and Carbon in some Natural Gases. *J. Geophys. Res.* **66 (**no.1.**)**, 277–306.

Appendix

Details on sampling locations; see Table A1. Parameters used for the diffusion coefficients see Table A2.

Table A1. Sample details.

Sample	Type	Mine	Shaft/ Level	sampling date	Depth km	T_s °C	ng	^{36}Cl	δD $\delta^{18}O$	Sample location
BE19BWBhDD13677	pw	Beatrix	1/9	28.03.01	1.050	–	x			40.8m exploration borehole, below the reef, sampled 2–4h after drilling
BE16FW-GDW #1	fw	Beatrix	1/6	16.03.01	0.866	34.0	x	x	x	G drive west, uncemented, 60m horizontal borehole, < 2 weeks old
BE16FW-GDW #3	fw	Beatrix	1/6	16.03.01	0.866	34.0	x			douplicate of BE16FW-GDW #1
BE16FW-IDW	fw	Beatrix	1/6	14.03.01	0.870	34.0		x	x	I drive west, 10-month-old borehole intersecting a water-bearing fault
BE23FW-A4RD	fw	Beatrix	2/23	13.03.01	0.718	33.5	x	x	x	crosscut A, reef drive, 6 month old water emanating borehole, high flow rate
BE24FW-C17W18 #2	fw	Beatrix	2/24	26.03.01	0.768	33.0	x	x	x	hanging wall borehole drilled into reef, intersecting Karoo-age dyke, actively mined stope
BE325FW-CTS	fw	Beatrix	3/25	27.03.01	1.300	39.0	x	x	x	borehole proximal to recently sunk shaft, formerly labeled "BE339FW-CTS"
BE327FW-CTS	fw	Beatrix	3/27	27.03.01	1.400	40.0	x	x	x	borehole proximal to recently sunk shaft, formerly labeled "BE340FW-CTS"
B2-25-FW1	*fw*	*Beatrix*	*2/25*	*05.12.98*	*1.000*	*35.0*	*x*	*x*	*x*	*noble gas sample contained high amounts of air-discarded as leaky*
E4-IPC-DW-2	gw	Driefontein	4/-	17.11.98	0.945	25.0	x	x	x	dolomite aquifer, valved borehole (3.6 MPa), Intermedediate Pump Compartment
E5-46-Bh1	fw	Driefontein	5/46	02.02.99	3.200	37.2	x	x	x	120 m subhorizontal borehole intersecting a high-pressure saline water pocket
EV522FW-HWD	fw	Evander	5/22	08.03.01	1.904	36.7	x	x	x	hanging wall drive in the Ventersdorp lavas
EV818FW-FBH	fw	Evander	8/18	21.06.01	1.830	45.0	x		x	same location as EV818FW-NEPD
EV818FW-NEPD	fw	Evander	8/18	06.03.01	1.830	45.0	x	x	x	north-east prospect drive, vertical borehole above reef, high flow rates
K4-41-FW1b	fw	Kloof	4/41	05.02.99	3.300	58.2	x			56 hanging wall drive south
K4-41-FW-2	fw	Kloof	4/41	05.02.99	3.300	52.4	x			56 hanging wall drive north, 3y old water emanating borehole
KL739FW	fw	Kloof	7/39	29.06.01	3.100	54.0	x		x	sampled from a three days old borehole intersecting a water bearing fracture
K4-41-FW-1	*fw*	*Kloof*	*4/41*	*08.12.98*	*3.300*	*60.0*	*x*	*x*	*x*	*noble gas sample contained high amounts of air-discarded as leaky*
W6-38-FW3 #1	*fw*	*Driefontein*	*6/38*	*26.11.98*	*2.700*	*45.0*	*x*			*noble gas sample contained high amounts of air-discarded as leaky*
W6-38-FW3 #2	*fw*	*Driefontein*	*6/38*	*26.11.98*	*2.700*	*45.0*	*x*			*noble gas sample contained high amounts of air-discarded as leaky*
WDF2b	fw	Driefontein	6/38	10.05.98	2.720	–		x	x	70m borehole drilled in 9/98, intersects water bearing fracture, initial flow rate: 3600L/hr
EV811FW-1XCA	fw	Evander	8/11	03.05.01	1.340	–		x		N1, crosscut A, total flow rate of about 3000 L/min,
E5-46-sump	ww	Driefontein	5/46	02.03.99	2.300	34.2		x	x	subsurface drainage basin, mix of service and fissure water
tap water, #2 shaft	tw	Beatrix	2/–	28.03.01	0.000	–		x		tap water from public water supply on Beatrix mine property

Details of the sample name, type of sample taken, origin, location, sampling date, depth, and sampling temperature T_s. The initial letters in the sample name reflect the same of the mine (BE = Beatrix, E = (East)Driefontein, W = (West)Driefontein, EV = Evander, K or KL = Kloof); pw stands for pore water, fw = fissure water, gw = ground water, ww = waste water from a surface reservoir and tw = tap water; cross symbols indicate the type of sample taken at a particular location; ng = noble gas sample, $^{36}C1$ = sample for $^{36}C1$-analysis, δD, $\delta^{18}O$ for stable isotope analysis of H_2O.

Table A2. Parameter for diffusion coefficients.

Gas	A [10^{-5}] cm^2/s	σ (Fit) [%] [10^{-5}] cm^2/s	Eα kJ/mol	σ (Eα) [%] kJ/mol
He	818	2,1	11,70	5
Ne	1608	3,5	14,84	8
^{36}Ar	(2023)	(5)	(16.32)	(10)
^{40}Ar	(2225)	(5)	(16.67)	(10)
Kr	6393	1,6	20,20	3
Xe	9007	3,5	21,61	5

Fit parameters A and Eα for experimentally determined diffusion coefficients for He, Ne, Kr and Xe in the temperature range of 5 to 35°C, (Jähne et al., 1986) $Dx(t) = A \cdot \exp(-E\alpha/RT)$, with x = He, Ne, Kr, Xe and T [K]. For Ar, first the diffusion coefficients for each of the given temperature in the range between 5 and 35°C are fitted from the given values for He, Ne, Kr and Xe, using the relation $D \sim 1/m^{0.5}$; then, the parameters for the diffusion coefficient are fitted from these data.